Mott-moiré excitons

Tsung-Sheng Huang,[1] Yang-Zhi Chou,[2,1] Christopher L. Baldwin,[1] Fengcheng Wu,[3,4] and Mohammad Hafezi[1,5]
[1]*Joint Quantum Institute, University of Maryland, College Park, Maryland 20742, USA*
[2]*Condensed Matter Theory Center, University of Maryland, College Park, Maryland 20742, USA*
[3]*Key Laboratory of Artificial Micro- and Nano-structures of Ministry of Education, and School of Physics and Technology, Wuhan University, Wuhan 430072, China*
[4]*Wuhan Institute of Quantum Technology, Wuhan 430206, China*
[5]*Pauli Center for Theoretical Studies, ETH Zurich, CH-8093 Zurich, Switzerland*

(Received 5 August 2022; revised 21 April 2023; accepted 24 April 2023; published 26 May 2023)

We develop a systematic theory for excitons subject to Fermi-Hubbard physics in moiré twisted transition metal dichalcogenides (TMDs). Specifically, we consider excitons from two moiré bands with a Mott-insulating valence band sustaining 120° spin order. These "Mott-moiré excitons," which are achievable in twisted TMD heterobilayers, are bound states of a magnetic polaron in the valence band and a free electron in the conduction band. We find significantly narrower exciton bandwidths in the presence of Hubbard physics, serving as a potential experimental signature of strong correlations. We also demonstrate the high tunability of Mott-moiré excitons through the dependence of their binding energies, diameters, and bandwidths on the moiré period. In addition, we study bound states between charges outside of the strongly correlated moiré band and find that these as well exhibit signatures of spin correlation. Our work provides guidelines for future exploration of strongly correlated excitons in triangular Hubbard systems such as twisted TMD heterobilayers.

DOI: 10.1103/PhysRevB.107.195151

I. INTRODUCTION

Two-dimensional (2D) semiconducting transition metal dichalcogenides (TMDs) [1–41] have become a rich platform with which to explore the interplay of optoelectronics and many-body physics, due primarily to their band structure properties such as infrared and visible-frequency band gaps [1] and additional valley degrees of freedom at low energy [2]. In particular, many studies have focused on the properties of excitons (bound states of electrons and holes) [3–10], and on understanding how excitons interact with the Fermi sea to form exciton-polarons [11–14,42]. In TMD *bilayers* [Fig. 1(a)], the relative twist angle between the two layers, and the resulting superlattice period, is a further tunable parameter [17–23,43]. The electronic properties of twisted TMD bilayers are very different from those of monolayers due to the presence of flat moiré bands that significantly enhance the role of many-body interactions, leading to strong correlations [24–38]. The effect of strong correlations on excitons in the presence of moiré structure remains a subject of active investigation.

One consequence of strong-correlation physics in twisted TMD bilayers is the emergence of correlated insulating states and charge order [24–38]. It has been pointed out that generalized moiré-Hubbard models can emerge for the first valence moiré band ($v1$) in heterobilayers [24] and for the first few valence moiré bands in homobilayers [25,26,30]. Moreover, at certain filling fractions ν (i.e., number of electrons per superlattice unit cell), these models predict the existence of correlated states such as Mott insulators ($\nu = 1$) and Wigner crystals ($\nu = \frac{1}{4}, \frac{1}{3}, \frac{1}{2}, \frac{2}{3}, \frac{3}{4}$) [27,30]. This explains several transport [31,32] and optical [31–33,36] measurements of TMD heterobilayers, which observe enhanced resistivity and incompressibility at the aforementioned filling fractions.

In addition to charge order, spin correlation [28,29,45,46] can significantly influence the properties of twisted TMD bilayers. For example, at half-filling and zero temperature, a triangular-lattice Hubbard model yields a 120° magnetically ordered state [24,47,48], and the spin fluctuations on top of such a background can strongly renormalize the charge dynamics, giving rise to magnetic polarons [49–51]. Intuitively, this is because the movement of charges in the ordered state disturbs the spin configuration, leaving a trail of misaligned spins that is energetically unfavored. To the best of our knowledge, conclusive signatures of spin ordering and magnetic polarons in twisted TMD bilayers have not been established experimentally, nor has the question been answered of how spin correlation affects the excitons.

The rich phenomena derived from the Hubbard model motivate us to study "Mott excitons" in twisted TMD bilayers, namely, excitons in which one or both of the charge constituents are magnetic polarons rather than bare charges. Broadly speaking, two distinct types of Mott excitons can exist. We coin them "intraband" and "interband" Mott excitons [see Fig. 1(b)].

Intraband Mott excitons consist of a vacancy and a double-occupancy within a single-band Hubbard model. Since the constituent charges lie within the same Bloch band, the lowest such excitonic state is optically dark (within the dipole approximation) and therefore not readily accessible in solid-state systems. A few theoretical works have considered this type of exciton [44,52–54], with particular focus on how spin fluctuations provide the binding mechanism [44], and despite the experimental challenges, certain indirect optical signatures

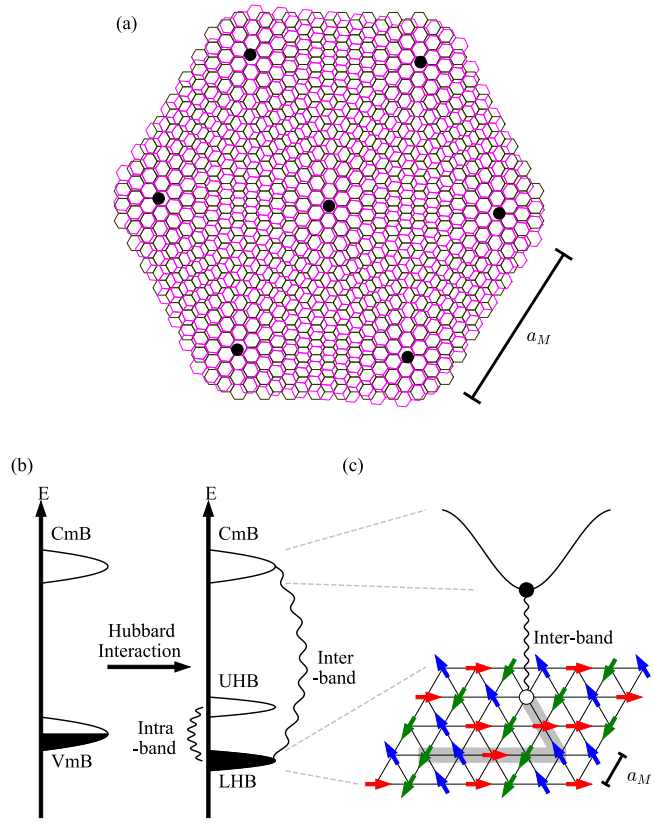

FIG. 1. Illustration of Mott-moiré excitons on the moiré superlattice of a TMD heterobilayer. (a) Moiré superlattice structure in a twisted TMD heterobilayer, for instance, $WSe_2/MoSe_2$ [24] or WSe_2/WS_2 bilayers [31]. Black dots indicate AA-stacked atoms which themselves define a triangular lattice structure and lead to folded moiré bands. (b) Schematic diagram of the first valence ($v1$) and conduction ($c1$) moiré bands. Vertical axes indicate energy, and the shaded area refers to the filled Fermi sea. The Hubbard interaction within the $v1$ band causes it to split into upper and lower Hubbard bands (UHB and LHB). Black wavy lines indicate interactions that can form Mott excitons, either intraband (hole in LHB and electron in UHB [44]) or interband (hole in LHB and electron in $c1$ band). The latter is the subject of this paper. (c) Schematic diagram for the inter-band Mott-moiré exciton. Black and white dots indicate the $c1$ electron and $v1$ hole, respectively. Red, green, and blue arrows show the 120° spin-ordered state on the triangular superlattice in the $v1$ band. Note that the trajectory of the hole, represented by gray shading, displaces spins and thus disturbs the spin order.

of intraband Mott excitons have recently been reported in iridates [55,56].

On the other hand, interband Mott excitons consist of a vacancy and electron in separate bands, with the valence band described by a Hubbard model and the conduction band otherwise empty. In this case, the binding mechanism has a direct Coulomb origin rather than being spin-mediated. These excitons very well can be optically bright, assuming the valence and conduction bands satisfy the appropriate selection rule. Accordingly, interband Mott excitons have recently been reported in cuprates via reflectivity measurements [57].

In this paper, we investigate the *inter*band Mott exciton formed from a magnetic polaron in the first valence moiré band ($v1$) and an electron in the first conduction moiré band ($c1$). We refer to these throughout as "Mott-moiré excitons." We give a theoretical description for the formation of Mott-moiré excitons with 120° spin order in $v1$ band, and discuss the role of spin correlation in determining their properties. In particular, we compare Mott-moiré excitons to those that would exist in the same band structure with the same Coulomb interaction but without any Mott physics (we label the latter simply as "moiré excitons"). Our main finding is that Mott-moiré excitons can be distinguished by their significantly heavier mass, which serves as a signature in diffusion measurements. Many of our techniques and conclusions hold equally well for Mott excitons in nonmoiré systems. Finally, complementing the study of Mott-moiré excitons, we also study bound states between charges outside the half-filled $v1$ band. We demonstrate that these "spectator excitons" are also sensitive to spin correlation, providing a potential experimental signature of spin physics in TMDs.

The outline of the paper is as follows. We summarize the model and our main results in Sec. II. We describe our theoretical techniques in Sec. III, and present our results in more detail in Sec. IV. Finally, we discuss potential experimental signatures of Mott-moiré excitons in Sec. V. Various technical details can be found in the Appendixes.

II. SUMMARY

A. Overview of the model

We consider Mott excitons in the presence of a moiré potential coming from a twisted TMD heterobilayer system [see Fig. 1(a)]. Stacking the two monolayers with a small relative twist angle gives the sample a moiré period a_M greater than the monolayer lattice spacings. This enlarged periodicity folds the band structure into minibands. It is known that a tight-binding model in terms of superlattice sites can describe both $c1$ and $v1$, albeit with strong onsite interactions in the latter at half-filling [24,35]. Such a filling condition is achievable by tuning the gate voltage [31]. Hence, we focus on a two-moiré-band model to capture the essence of interband Mott excitons:

$$\begin{aligned}\hat{H} = &-t\sum_{\tau}\sum_{\langle \boldsymbol{R},\boldsymbol{R}'\rangle}[\hat{c}^{\dagger}_{\boldsymbol{R},\tau}\hat{c}_{\boldsymbol{R}',\tau}+\hat{h}^{\dagger}_{\boldsymbol{R},\tau}\hat{h}_{\boldsymbol{R}',\tau}]\\ &+U\sum_{\boldsymbol{R}}\hat{n}_{\boldsymbol{R},\uparrow}\hat{n}_{\boldsymbol{R},\downarrow}\\ &-\sum_{\tau\tau'}\sum_{\boldsymbol{R}\boldsymbol{R}'}V_{|\boldsymbol{R}-\boldsymbol{R}'|}\hat{c}^{\dagger}_{\boldsymbol{R},\tau}\hat{h}^{\dagger}_{\boldsymbol{R}',\tau'}\hat{h}_{\boldsymbol{R}',\tau'}\hat{c}_{\boldsymbol{R},\tau},\end{aligned} \tag{1}$$

with $\tau\in\{\uparrow,\downarrow\}$ labeling the spin index [58], and $\langle \boldsymbol{R},\boldsymbol{R}'\rangle$ denoting nearest-neighbor sites on a triangular superlattice. $\hat{c}_{\boldsymbol{R},\tau}$ represents the $c1$-electron annihilation operator and $\hat{h}_{\boldsymbol{R},\tau}$ the $v1$-hole operator. We assume that the charges live on the same triangular superlattice, although they could lie on different lattices microscopically [19]. $\hat{n}_{\boldsymbol{R},\tau}\equiv 1-\hat{h}^{\dagger}_{\boldsymbol{R},\tau}\hat{h}_{\boldsymbol{R},\tau}$ is the *electron* occupation at moiré site $\boldsymbol{R}$ and spin τ in $v1$. Note that, as discussed above, we only include the Hubbard interaction U for electrons in $v1$, specifically onsite repulsion since the off-site electrostatic interactions can be rendered insignificant by gate screening [24]. We choose the $v1$-hole and $c1$-electron

hopping coefficients t to be equal for simplicity, and assume $U \gg t$ [24]. Lastly, $V_{|\boldsymbol{R}-\boldsymbol{R}'|}$ denotes the Coulomb interaction between the two moiré bands. Since the $v1$ is in a (correlated) insulating state and the $c1$ is initially empty, the interaction is not screened.

In TMD heterobilayers, typically Coulomb interaction is more significant than the moiré bandwidths [24,59,60]. Although such a considerable interband attraction could mix the narrow minibands, experiments suggest that these single-particle bands still manifest in optical excitations [61]. Thus, we can focus on specific moiré bands and use Eq. (1) as a minimum model to capture strong correlation physics.

In addition to the density-density attraction in Eq. (1), other interband interactions are present in general. These contributions include exchange Coulomb interaction and optical coupling [62,63]. We drop such terms in Eq. (1) since large band gaps (of order eV [1]) in TMDs diminish their correction to the exciton energy [62]. In particular, the $C3$ rotational symmetry completely suppresses the interband exchange process within bright Mott-moiré excitons (see Appendix H and Refs. [5,64]). We thus neglect the exchange interaction and optical coupling in our minimum model.

With the two-band model of Eq. (1), we proceed to describe the resulting spin correlation in $v1$. Following the standard arguments [65], including extra charges (in our case vacancies) into the half-filled $v1$ band yields an effective t-J model. We take the 120° coplanar spin-ordered phase of such a model as our ground state [24], supported by measurements showing antiferromagnetic Curie-Weiss behavior at half-filling of the moiré valence band [31]. Spin fluctuations on top of such order propagate at energy scale $J \simeq 4t^2/U$ [24] and dress the charges into magnetic polarons [49–51]. It is convenient to describe the charge and spin degrees of freedom separately, via slave-fermion [49,66] and Holstein-Primakoff bosons [65], respectively. This reduces Eq. (1) to the following two-body Hamiltonian (see Sec. III):

$$\hat{H} = \sum_{\boldsymbol{k}} \epsilon_{\boldsymbol{k}} \hat{\psi}^\dagger_{\boldsymbol{k}} \hat{\psi}_{\boldsymbol{k}} - 2t \sum_{\boldsymbol{k},\tau} \gamma_{\boldsymbol{k}} \hat{c}^\dagger_{\boldsymbol{k},\tau} \hat{c}_{\boldsymbol{k},\tau} - \frac{1}{\mathcal{A}} \sum_{\tau} \sum_{\boldsymbol{k},\boldsymbol{k}',\boldsymbol{q}} V(q) \hat{c}^\dagger_{\boldsymbol{k}+\boldsymbol{q},\tau} \hat{\psi}^\dagger_{\boldsymbol{k}'-\boldsymbol{q}} \hat{\psi}_{\boldsymbol{k}'} \hat{c}_{\boldsymbol{k},\tau}, \tag{2}$$

in which $\hat{\psi}$ stands for the fermionic charge degree of freedom (i.e., holon) in $v1$ band, whereas $\hat{c}$ remains the bare $c1$ electron. $\mathcal{A}$ denotes the system area. Momentum sums run over the first moiré Brillouin zone (mBZ). $\epsilon_{\boldsymbol{k}}$ is the (dressed) holon dispersion, $-2t\gamma_{\boldsymbol{k}}$ is the $c1$ electron dispersion, and $V(q)$ is the Coulomb interaction written in momentum space. See Eqs. (24), (16), and (26) for the explicit expressions and further details.

Equation (2) captures the formation of Mott-moiré excitons from $c1$ electrons and $v1$ holons [see also Fig. 1(b)]. We introduce the composite operator $\hat{X}_{n,\tau}(\boldsymbol{Q})$ for such a bound state, which we write in the form

$$\hat{X}_{n,\tau}(\boldsymbol{Q}) = \sum_{\boldsymbol{p}} \phi^{(n)}_{\boldsymbol{Q}}(\boldsymbol{p}) \hat{\psi}_{\frac{\boldsymbol{Q}}{2}-\boldsymbol{p}} \hat{c}_{\frac{\boldsymbol{Q}}{2}+\boldsymbol{p},\tau}, \tag{3}$$

where $\boldsymbol{Q}$ and $\boldsymbol{p}$ are the total and relative momenta of the two particles, respectively, and n labels the internal state. $\phi^{(n)}_{\boldsymbol{Q}}(\boldsymbol{p})$ is the corresponding exciton wave function, and if chosen so as to solve an appropriate effective two-particle Schrödinger equation [Eq. (27)], Eq. (2) becomes "quadratic" in terms of the composite operators:

$$\hat{H} = \sum_{n,\boldsymbol{Q},\tau} E^X_{n,\boldsymbol{Q}} \hat{X}^\dagger_{n,\tau}(\boldsymbol{Q}) \hat{X}_{n,\tau}(\boldsymbol{Q}), \tag{4}$$

with $E^X_{n,\boldsymbol{Q}}$ denoting the exciton energy. The operator $\hat{X}_{n,\tau}(\boldsymbol{Q})$ can be shown to satisfy bosonic commutation relations in the dilute limit [63] (with a correction proportional to the exciton density [67]), meaning that Eq. (4) does amount to an approximate diagonalization of the Hamiltonian for small numbers of excitons.

We end this overview by noting that, strictly speaking, Eq. (3) gives such bound state as a composite particle involving a *holon* rather than magnetic polaron [68]. The holon is merely the charge sector of the polaron: the latter additionally contains a surrounding cloud of spin fluctuations [49,69]. Yet since we shall find that the exciton radius (Fig. 3) is smaller than the polaron radius [69], we feel it is reasonable to consider binding between the electron and holon alone (spin fluctuations are still included via the dressed holon dispersion).

B. Overview of results

Our main finding is that moiré and Mott-moiré excitons are similar in certain regards (namely, the binding energy and radius) but dramatically different in others (particularly the bandwidth, i.e., exciton mass). We further identify how the properties of the two vary with the moiré period a_M: recall that the moiré period is tunable experimentally.

To begin, the dispersions of moiré and Mott-moiré excitons are quite different, as shown in Fig. 2. Whereas moiré excitons possess a band minimum at $\boldsymbol{Q} = \Gamma \equiv (0, 0)$ and maxima at the mBZ boundary, Mott-moiré excitons have the opposite behavior: a maximum at $\boldsymbol{Q} = \Gamma$ and minima at the mBZ boundary. We shall demonstrate that the inverted dispersion is precisely a consequence of the background spin order. Furthermore, the bandwidth W_X of Mott-moiré excitons is roughly two orders of magnitude smaller than that of moiré excitons [see Fig. 3(c)]. This suppression is primarily due to the reduced holon bandwidth, and experiments in cold-atom quantum simulators have reported similar effects [70]. Interestingly, in a sense we shall make sharp, the lowered holon bandwidth is more a consequence of spin *fluctuations* than spin order alone. We refer to Sec. IV for more details.

Mott-moiré excitons have a slightly smaller binding energy [71] $E^B_{n,\boldsymbol{Q}}$ and larger diameter $\langle r \rangle_X$ compared to moiré excitons in their lowest internal states ($n = 0$) [see Figs. 3(a) and 3(b)]. Regardless, in both cases the exciton is significantly smaller than a moiré period, and correspondingly the binding energy is much greater than the Coulomb energy scale for charges separated by a_M. Qualitatively, this is due to the fact that the onsite Coulomb attraction is noticeably larger than the superlattice hopping amplitudes (see Fig. 11). In reality, exciton sizes could deviate from Fig. 3(b) since a description of the dynamics within a supercell is beyond our two-band model (1). Nevertheless, we still anticipate that the separation between charges in the lowest exciton will be less than a

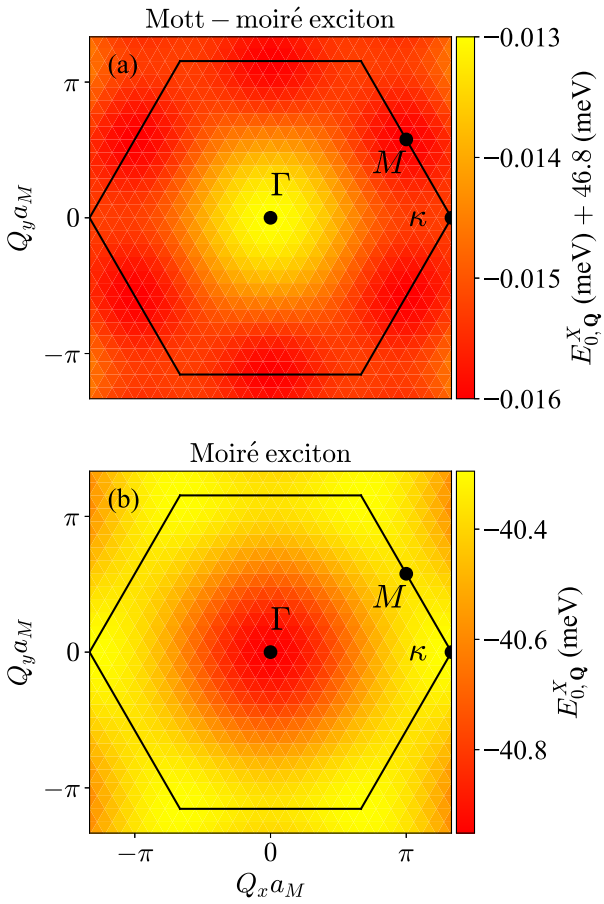

FIG. 2. Dispersion relation of the lowest-energy throughout the entire mBZ, indicated by the black hexagon for Mott-moiré (top) and moiré (bottom) exciton, at superlattice period $a_M = 10$ nm and with dielectric constant $\epsilon_r = 10$. For Mott-moiré, we use $t/J = 7.3$ (taken from Ref. [24]) and the equilibrium magnetization $m = 0.48$. System size is 3×24^2 sites. Q_x and Q_y are the total momentum of the two-particle state. Color bars indicate energy relative to the two-particle continuum (lowest energy of two free particles); note in particular that the top panel has energies shifted by 46.8 meV. Black dots indicate important points in the Brillouin zone.

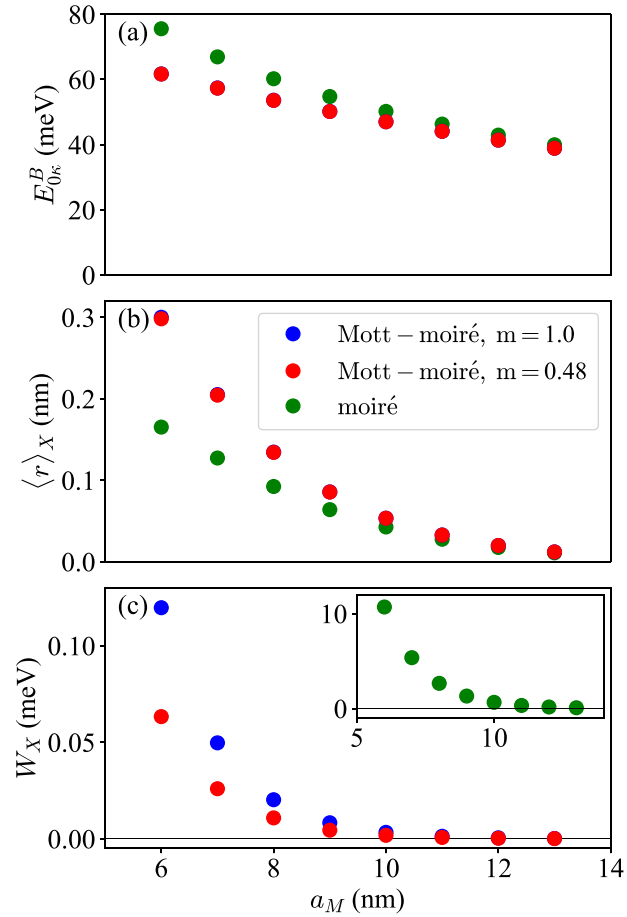

FIG. 3. Properties of Mott-moiré excitons at different magnetization (blue and red, indistinguishable at the scales of top and middle panels) and moiré excitons (green) as functions of the moiré period a_M. Dielectric constant is $\epsilon_r = 10$. System size is $N = 3\times24^2$ sites. (a) Binding energy of the lowest internal state $E^B_{0,\kappa}$ at total momentum $\boldsymbol{Q} = \boldsymbol{\kappa}$, which has the largest binding among all $\boldsymbol{Q}$ for both excitons (even though the moiré exciton energy is lower at $\boldsymbol{Q} = \Gamma$ in absolute numbers). Note that our binding energy is of the same order of magnitude as in the literature [60]. (b) Average diameter of excitons at total momentum κ. (c) Exciton bandwidths W_X. Inset shares the same axes. Values for t and J as functions of a_M are taken from Ref. [24] for WSe_2 on top of $MoSe_2$ (see also Fig. 17).

moiré period, even for a multiband calculation, as long as the bandwidths of incorporated minibands are narrower than the strong Coulomb interaction. Such a conclusion is consistent with first-principle calculations [19] and identifies the bound states as Frenkel type [72], unlike the Wannier-type excitons (size larger than lattice spacing) found in conventional semiconductors [73]. We provide the corresponding analysis in Sec. IV (with further details in Appendix G).

As for how these properties vary with the moiré period a_M, a larger period implies significantly suppressed superlattice hopping amplitudes and thus relatively stronger Coulomb binding. This explains the trends seen in Fig. 3: $\langle r \rangle_X$ and W_X both decrease as a_M increases. Since the intersite Coulomb interaction is itself weaker at larger a_M, albeit less so than the hopping strength, the binding energy $E^B_{0\kappa}$ decreases as well. We refer to Sec. IV and Appendix G for more details.

We also compare the Mott-moiré exciton properties at different sublattice magnetizations m (the order parameter for the 120° coplanar spin state). As we are considering 2D systems, spin fluctuations reduce the magnetization even at zero temperature. Linear spin-wave theory predicts $m \approx 0.48$ on the triangular lattice, which we compare to full magnetization $m = 1$. The qualitative trends for all properties are the same at both magnetizations. Furthermore, we see in Fig. 3 that only the exciton bandwidth has a noticeable dependence on m (and even then only by a factor of 2). This is because m influences only the holon kinetic energy, which is a small energy scale regardless [see Fig. 4]. Thus, while the exciton bandwidth (being controlled primarily by the holon bandwidth) is sensitive to magnetization, the other properties (for which the holon acts more or less as inert) are not.

In addition, we study the excited states of Mott-moiré excitons within the two-band model of Eq. (2). In accordance with the symmetry group of this model, we identify nondegenerate

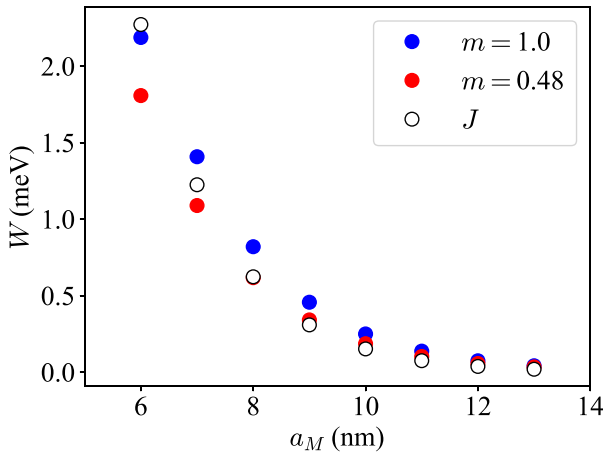

FIG. 4. Dressed holon bandwidth W from SCBA as a function of moiré period a_M, at different sublattice magnetizations m (blue and red). System size is 3×24^2 sites. Also shown is J as a function of a_M (empty circle), for WSe_2 on top of $MoSe_2$ according to Ref. [24].

states classified as s and f wave, and doubly degenerate p- and d-wave-like states. However, we find that only s-wave excitons are optically bright [see Eq. (30)] and that the oscillator strength comes mainly from the lowest state (see Fig. 13). Although these results are based on a two-band model, we expect that the analysis can be generalized to multiband models.

Lastly, we note that our Mott-moiré exciton results are based on the existence of 120° coplanar spin order. While supported by the measurements exhibiting antiferromagnetic Curie-Weiss behavior [31], concrete signatures of such correlation are absent. Our main result, i.e., suppressed exciton bandwidth in the presence of spin physics, serves as an additional signature. As a complement, we discuss another way of probing spin correlation by utilizing *spectator excitons* in Sec. IV C and Appendix I.

III. FORMALISM AND METHODS

In this section, we present the formalism describing interband Mott-moiré excitons in TMD heterobilayers. The Hubbard model on a triangular lattice has been investigated with various analytical methods: Hartree-Fock mean-field theory [74], strong-coupling expansions [75], and slave particles [47,48]. Here we use the slave-particle formalism because spin and charge excitations are automatically distinguished in this approach. The steps of our calculations are summarized as follows:

(1) Implement projection to the subspace of zero double occupancies in $v1$ band and keep only nearest-neighbor terms, thus obtaining a t-J model [24,65].

(2) Express the Hamiltonian in terms of slave particles, namely, holons and spinons (keep in mind that the spin degrees of freedom described by spinons are locked to the valley degrees of freedom).

(3) Focus on the 120° coplanar magnetically ordered phase of the triangular-lattice t-J model, as described through a mean-field approximation for the spinons (while still including linear spin-wave fluctuations).

(4) Calculate the dispersion of spin-dressed holons within the self-consistent Born approximation (SCBA) [47–49,66].

(5) Construct the exciton Hamiltonian from the kinetic energies of dressed holons in $v1$ and electrons in $c1$, together with the Coulomb interaction. Diagonalize this Hamiltonian numerically to obtain the exciton spectrum and wave functions.

Before proceeding, let us emphasize that our usage of mean-field theory to describe the magnetic order implies that our results become inaccurate near its melting point. We nonetheless expect mean-field theory to capture the qualitative features of the 120° spin-ordered phase, and previous studies have confirmed that magnetic order persists (at around 0.4–0.5 of the classical value) even once quantum fluctuations are taken into account [76–78]. Furthermore, our results turn out to be largely insensitive to the precise value of the magnetization (see Sec. II).

A. t-J model

Since the derivation of a t-J model from a half-filled Hubbard model is by now standard (see, e.g., Ref. [65]), we simply mention the result. Starting from a state with one $v1$ electron per superlattice site, second-order perturbation theory in t/U gives an effective Hamiltonian:

$$\hat{H}_{\rm tJ} = -t\sum_{\tau}\sum_{\langle \boldsymbol{R},\boldsymbol{R}'\rangle} \hat{\mathcal{P}}\hat{h}^{\dagger}_{\boldsymbol{R},\tau}\hat{h}_{\boldsymbol{R}',\tau}\hat{\mathcal{P}} + \hat{H}_J, \tag{5}$$

$$\hat{H}_J = J\sum_{\langle \boldsymbol{R},\boldsymbol{R}'\rangle} \hat{\boldsymbol{S}}_{\boldsymbol{R}}\cdot\hat{\boldsymbol{S}}_{\boldsymbol{R}'}, \quad \hat{\boldsymbol{S}}_{\boldsymbol{R}} \equiv \sum_{\tau\tau'}\hat{h}_{\boldsymbol{R},\tau}\frac{\boldsymbol{\sigma}_{\tau,\tau'}}{2}\hat{h}^{\dagger}_{\boldsymbol{R},\tau'}, \tag{6}$$

where $J \equiv 4t^2/U$, $\hat{\mathcal{P}}$ is the projector onto the subspace having no more than one electron per site, and $\boldsymbol{\sigma}_{\tau,\tau'}$ denotes the vector of 2×2 Pauli matrices.

B. Slave particles

The hole creation operator can be represented as (meaning that the two sides obey the same commutation relations)

$$\hat{h}^{\dagger}_{\boldsymbol{R},\tau} = \hat{\psi}^{\dagger}_{\boldsymbol{R}}\hat{s}_{\boldsymbol{R},\tau} + \tau\hat{s}^{\dagger}_{\boldsymbol{R},-\tau}\hat{d}_{\boldsymbol{R}}, \tag{7}$$

with fermionic $\hat{\psi}_{\boldsymbol{R}}$ and $\hat{d}_{\boldsymbol{R}}$, and bosonic $\hat{s}_{\boldsymbol{R},\tau}$. We interpret $\hat{\psi}_{\boldsymbol{R}}$ as an empty site, a "holon," and $\hat{s}_{\boldsymbol{R},\tau}$ as a singly occupied site with spin (equivalently valley), a "spinon" [79–81]. $\hat{d}_{\boldsymbol{R}}$ corresponds to a doubly occupied site, but since the t-J model projects into the subspace with no double occupancies, this operator does not appear in any subsequent expressions [it is needed only to ensure that Eq. (7) is consistent with the commutation relations]. The slave-particle transformation is illustrated in Fig. 5.

Equation (7) indicates that hole creation (i.e., electron annihilation) is equivalent to removing the corresponding spinon and creating a holon in its place (or replacing a double occupancy with the nonannihilated spin). Since we are neglecting double occupancies, any site which does not contain a spin by definition contains a hole, and therefore the slave particles must obey the following constraints for all $\boldsymbol{R}$:

$$\hat{\psi}^{\dagger}_{\boldsymbol{R}}\hat{\psi}_{\boldsymbol{R}} + \sum_{\tau}\hat{s}^{\dagger}_{\boldsymbol{R}\tau}\hat{s}_{\boldsymbol{R}\tau} = 1, \quad \hat{d}^{\dagger}_{\boldsymbol{R}}\hat{d}_{\boldsymbol{R}} = 0. \tag{8}$$

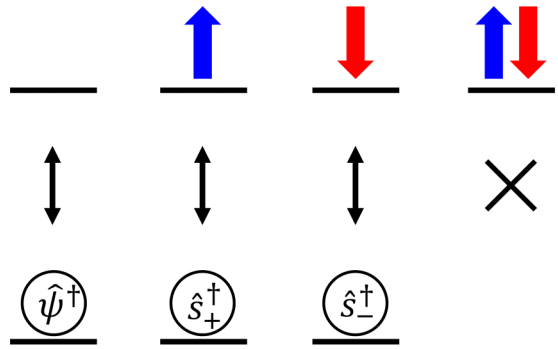

FIG. 5. Schematic diagram for the slave-particle formalism. Blue and red arrows represent the states with a single $\tau = \uparrow$ and $\tau = \downarrow$ electron, respectively, and are mapped to states with the corresponding bosonic spinons $\hat{s}$. States with zero and two electrons are mapped to corresponding fermionic slave particles, holons $\hat{\psi}$, and doublons $\hat{d}$. Doublons are not shown, as indicated by the cross, because they are projected out due to the large energy cost U.

Substituting Eq. (7) into (5) and making use of the constraints allows us to express $\hat{H}_{tJ}$ as $\hat{H}_t + \hat{H}_J$, where

$$\hat{H}_t = -t \sum_{\tau} \sum_{\langle \boldsymbol{R}, \boldsymbol{R}' \rangle} (\hat{\psi}^\dagger_{\boldsymbol{R}} \hat{\psi}_{\boldsymbol{R}'} \hat{s}^\dagger_{\boldsymbol{R}',\tau} \hat{s}_{\boldsymbol{R},\tau} + \text{H.c.}), \tag{9}$$

$$\hat{H}_J = J \sum_{\langle \boldsymbol{R}, \boldsymbol{R}' \rangle} \hat{\boldsymbol{\mathcal{S}}}_{\boldsymbol{R}} \cdot \hat{\boldsymbol{\mathcal{S}}}_{\boldsymbol{R}'}, \quad \hat{\boldsymbol{\mathcal{S}}}_{\boldsymbol{R}} = \sum_{\tau\tau'} \hat{s}^\dagger_{\boldsymbol{R},\tau} \frac{\hat{\boldsymbol{\sigma}}_{\tau,\tau'}}{2} \hat{s}_{\boldsymbol{R},\tau'}, \tag{10}$$

where the spin vectors are now expressed in terms of spinons. Note that the Hamiltonian automatically preserves the conditions in Eq. (8).

C. Magnetic order and spin waves

To study the magnetic order in the t-J model, we consider the dilute limit in which the low number of holons does not disturb the spin background. Consequently, $\hat{H}_J$ alone determines the spin ground state of $\hat{H}_{tJ}$. In the classical limit, $\hat{H}_J$ is minimized by a 120° spin order such as sketched in Fig. 7. Replacing $\hat{\boldsymbol{\mathcal{S}}}_{\boldsymbol{R}}$ by $\langle \hat{\boldsymbol{\mathcal{S}}}_{\boldsymbol{R}} \rangle = \frac{\langle \hat{\boldsymbol{\sigma}}_{\boldsymbol{R}} \rangle}{2}$, this classical order on the A, B, and C sublattices reads as

$$\langle \hat{\boldsymbol{\sigma}}_{\boldsymbol{R}} \rangle \equiv \hat{\boldsymbol{n}}_{\boldsymbol{R}} = \begin{cases} \boldsymbol{e}_x, & \boldsymbol{R} \in A \\ -\frac{\boldsymbol{e}_x}{2} - \frac{\sqrt{3}\boldsymbol{e}_y}{2}, & \boldsymbol{R} \in B \\ -\frac{\boldsymbol{e}_x}{2} + \frac{\sqrt{3}\boldsymbol{e}_y}{2}, & \boldsymbol{R} \in C. \end{cases} \tag{11}$$

To include a low density of spin fluctuations on top of this background order, we rewrite the spinons $\hat{s}_{\boldsymbol{R},\tau}$ in terms of Holstein-Primakoff (HP) bosons $\hat{a}_{\boldsymbol{R}}$ [65]:

$$\hat{U}_{\boldsymbol{R}} \begin{bmatrix} \hat{s}_{\boldsymbol{R}\uparrow} \\ \hat{s}_{\boldsymbol{R}\downarrow} \end{bmatrix} = \begin{bmatrix} \sqrt{2S - \hat{a}^\dagger_{\boldsymbol{R}} \hat{a}_{\boldsymbol{R}}} \\ \hat{a}_{\boldsymbol{R}} \end{bmatrix}. \tag{12}$$

Here $\hat{U}_{\boldsymbol{R}}$ is the spin rotation matrix from $\boldsymbol{e}_z$ to $\hat{\boldsymbol{n}}_{\boldsymbol{R}}$. S denotes the spin magnitude. Although we are ultimately considering $S = \frac{1}{2}$, it is useful to compare with the semiclassical regime $S \gg 1$ [65]. Magnetic order in this calculation is characterized by the (normalized) sublattice magnetization:

$$m \equiv \left[1 - \frac{1}{S} \langle \hat{a}^\dagger_{\boldsymbol{R}} \hat{a}_{\boldsymbol{R}} \rangle \right]. \tag{13}$$

We refer to Appendix B for further details.

Thus far, all transformations have been exact (except for the perturbation theory used to derive the t-J model). To make further progress, we consider either of two similar approximations. First is the standard linear spin-wave (LSW) theory [47–49,65], namely, expanding in $1/S$ and neglecting all subleading terms. Even though $S = \frac{1}{2}$ is far from the large-S limit, it has been observed that this approximation still gives the correct qualitative features of spin waves [82,83]. Second is a mean-field approximation in which we replace $\sqrt{2S - \hat{a}^\dagger_{\boldsymbol{R}} \hat{a}_{\boldsymbol{R}}}$ in Eq. (12) by $\xi \equiv \sqrt{2S - \frac{1}{N} \sum_{\boldsymbol{R}} \langle \hat{a}^\dagger_{\boldsymbol{R}} \hat{a}_{\boldsymbol{R}} \rangle}$, where the expectation value is in the ground state of $\hat{H}_J$. The value $\langle \hat{a}^\dagger_{\boldsymbol{R}} \hat{a}_{\boldsymbol{R}} \rangle$ is then determined self-consistently.

Both approaches ultimately approximate $\hat{H}_J$ by a quadratic Hamiltonian, which a Bogoliubov rotation then diagonalizes. The resulting expression is, in terms of momenta $\boldsymbol{q}$,

$$\hat{H}_J = \frac{3J\xi^2}{2} \sum_{\boldsymbol{q}} \Omega_{\boldsymbol{q}} \hat{\beta}^\dagger_{\boldsymbol{q}} \hat{\beta}_{\boldsymbol{q}}, \quad \hat{\beta}_{\boldsymbol{q}} \equiv u_{\boldsymbol{q}} \hat{a}_{\boldsymbol{q}} - v_{\boldsymbol{q}} \hat{a}^\dagger_{-\boldsymbol{q}}, \tag{14}$$

where

$$\Omega_{\boldsymbol{q}} = \sqrt{\left(1 + \frac{\gamma_{\boldsymbol{q}}}{6}\right)^2 - \frac{\gamma^2_{\boldsymbol{q}}}{4}}, \tag{15}$$

$$\gamma_{\boldsymbol{q}} = \sum_{i=1}^{3} \cos(a_M \boldsymbol{q} \cdot \boldsymbol{e}_i), \tag{16}$$

$$u_{\boldsymbol{q}} = \sqrt{\frac{1}{2\Omega_{\boldsymbol{q}}} \left(1 + \frac{\gamma_{\boldsymbol{q}}}{6} + \Omega_{\boldsymbol{q}}\right)}, \tag{17}$$

$$v_{\boldsymbol{q}} = \text{sgn}[\gamma_{\boldsymbol{q}}] \sqrt{\frac{1}{2\Omega_{\boldsymbol{q}}} \left(1 + \frac{\gamma_{\boldsymbol{q}}}{6} - \Omega_{\boldsymbol{q}}\right)}, \tag{18}$$

with $\boldsymbol{e}_1 = \boldsymbol{e}_x$ and $\boldsymbol{e}_{2,3} = -\boldsymbol{e}_x/2 \pm \sqrt{3}\boldsymbol{e}_y/2$ ($\boldsymbol{e}_x$ and $\boldsymbol{e}_y$ are the x and y unit vectors). LSW theory corresponds to $\xi^2 = 1$, while the mean-field approximation corresponds to $\xi^2 = (1 + m)S$ [see Eq. (13)]. In particular, one finds that $m = 1 - \frac{2}{N} \sum_{\boldsymbol{q}} v^2_{\boldsymbol{q}} \simeq 0.48$ at zero temperature, independent of t and U (see Appendix B).

Making the same approximations in $\hat{H}_t$ gives (N denotes the number of moiré sites)

$$\hat{H}_t = t\xi^2 \sum_{\boldsymbol{k}} \gamma_{\boldsymbol{k}} \hat{\psi}^\dagger_{\boldsymbol{k}} \hat{\psi}_{\boldsymbol{k}} + \frac{\sqrt{3}t\xi}{\sqrt{N}} \sum_{\boldsymbol{k},\boldsymbol{q}} [i M_{\boldsymbol{k},\boldsymbol{q}} \hat{\psi}^\dagger_{\boldsymbol{k}+\boldsymbol{q}} \hat{\psi}_{\boldsymbol{k}} \hat{\beta}^\dagger_{-\boldsymbol{q}} + \text{H.c.}], \tag{19}$$

with vertex

$$M_{\boldsymbol{k},\boldsymbol{q}} = h_{\boldsymbol{k}} v_{\boldsymbol{q}} - h_{\boldsymbol{k}+\boldsymbol{q}} u_{\boldsymbol{q}}, \tag{20}$$

$$h_{\boldsymbol{k}} \equiv \sum_{i=1}^{3} \sin(a_M \boldsymbol{k} \cdot \boldsymbol{e}_i). \tag{21}$$

Note that the bare holon hopping in Eq. (19) has the opposite sign compared to that of the original hole, which is $-2t\gamma_{\boldsymbol{k}} \hat{h}^\dagger_{\boldsymbol{k},\tau} \hat{h}_{\boldsymbol{k},\tau}$ [Eq. (5)]. The minus sign comes from the fact that holon hopping has an additional factor of the dot product between neighboring spin axes [see Eq. (9)], which

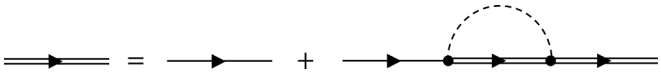

FIG. 6. Diagrammatic equation defining the self-consistent Born approximation (SCBA) for the holon propagator. Solid single lines are the bare holon propagator $G^0_k(\epsilon)$. Solid double lines are the dressed holon propagator $G_k(\epsilon)$. The dashed line represents the propagator for a Holstein-Primakoff spin excitation, and black dots indicate the holon-spin vertex [second line of Eq. (19)].

is $\cos 2\pi/3 = -\frac{1}{2}$ for 120° order. Depletion of the magnetization due to spin fluctuations gives a further factor ξ^2.

D. Self-consistent Born approximation

The second term of Eq. (19) leads to a modification of the holon propagator, which we describe via the standard self-consistent Born approximation (SCBA) [47–49] as given in Fig. 6. The SCBA ignores vertex corrections and crossed diagrams, and uses the bare spin propagator corresponding to Eq. (14). Figure 6 translates to the integral equation

$$\Sigma_{\boldsymbol{k}}(\epsilon) = \frac{3t^2\xi^2}{N}\sum_{\boldsymbol{q}} \frac{M^2_{\boldsymbol{k},\boldsymbol{q}}}{\epsilon - \omega_{\boldsymbol{q}} - t\xi^2\gamma_{\boldsymbol{k}+\boldsymbol{q}} - \Sigma_{\boldsymbol{k}+\boldsymbol{q}}(\epsilon-\omega_{\boldsymbol{q}})}, \tag{22}$$

where $\Sigma_{\boldsymbol{k}}(\epsilon)$ is the dressed holon self-energy. We solve Eq. (22) numerically and determine the effective holon dispersion $\epsilon_{\boldsymbol{k}}$ by locating a pole in the propagator [which amounts to solving $\Sigma_{\boldsymbol{k}}(\epsilon_{\boldsymbol{k}}) + t\xi^2\gamma_{\boldsymbol{k}} = \epsilon_{\boldsymbol{k}}$].

We find that, in practice, the effective holon dispersion can be approximated reasonably well by that of the following effective Hamiltonian:

$$\hat{H}_{\text{d.h.}} = -\sum_{\boldsymbol{R}}\sum_{i=1}^{3}[t_1\hat{\psi}^\dagger_{\boldsymbol{R}}\hat{\psi}_{\boldsymbol{R}+\boldsymbol{e}_i} + t_2\hat{\psi}^\dagger_{\boldsymbol{R}}\hat{\psi}_{\boldsymbol{R}+\boldsymbol{e}'_i} + t_3\hat{\psi}^\dagger_{\boldsymbol{R}}\hat{\psi}_{\boldsymbol{R}+2\boldsymbol{e}_i}] + \text{H.c.}, \tag{23}$$

where $\boldsymbol{e}_i$ are again the nearest-neighbor vectors defined below Eq. (18), and $\boldsymbol{e}'_i$ are next-nearest-neighbor vectors: $\boldsymbol{e}'_1 = \sqrt{3}\boldsymbol{e}_y$ and $\boldsymbol{e}'_{2,3} = \pm\frac{3}{2}\boldsymbol{e}_x - \frac{\sqrt{3}}{2}\boldsymbol{e}_y$. The dispersion corresponding to Eq. (23) is

$$\epsilon_{\boldsymbol{k}} = -2t_1\gamma_{\boldsymbol{k}} - 2t_2\gamma'_{\boldsymbol{k}} - 2t_3\gamma_{2\boldsymbol{k}}, \tag{24}$$

where $\gamma'_k = \sum_{i=1}^{3}\cos(a_M\boldsymbol{k}\cdot\boldsymbol{e}'_i)$.

Equations (23) and (24) have a simple physical interpretation: in addition to the original nearest-neighbor hopping (with renormalized amplitude t_1), there is effective hopping to next-nearest-neighbor sites, which can be either to the same or different sublattices (with amplitudes t_2 and t_3, respectively). This is illustrated in Fig. 7. In our subsequent calculations, we use $\epsilon_{\boldsymbol{k}}$ as given by Eq. (24) for the holon dispersion, with the hopping amplitudes determined by a fit to the numerical solution of Eq. (22).

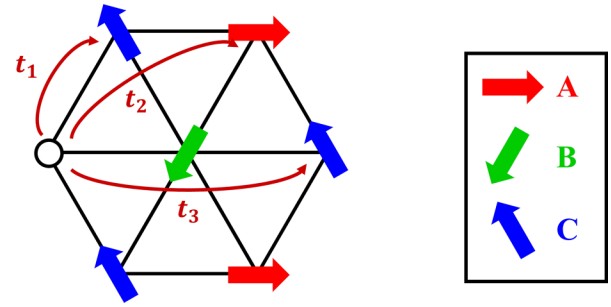

FIG. 7. Illustration of hopping parameters t_1, t_2, and t_3 for the approximated dressed-holon dispersion in Eq. (24). Arrows show the background magnetic order in which the holon (white dot) hops.

E. Exciton Hamiltonian

Recall the effective Hamiltonian given in Eq. (2) of Sec. II (reproduced here):

$$\hat{H} = \sum_{\boldsymbol{k}}\epsilon_{\boldsymbol{k}}\hat{\psi}^\dagger_{\boldsymbol{k}}\hat{\psi}_{\boldsymbol{k}} - 2t\sum_{\boldsymbol{k},\tau}\gamma_{\boldsymbol{k}}\hat{c}^\dagger_{\boldsymbol{k},\tau}\hat{c}_{\boldsymbol{k},\tau} - \frac{1}{\mathcal{A}}\sum_{\tau}\sum_{\boldsymbol{k},\boldsymbol{k}',\boldsymbol{q}}V(q)\hat{c}^\dagger_{\boldsymbol{k}+\boldsymbol{q},\tau}\hat{\psi}^\dagger_{\boldsymbol{k}'-\boldsymbol{q}}\hat{\psi}_{\boldsymbol{k}'}\hat{c}_{\boldsymbol{k},\tau}. \tag{25}$$

The preceding subsections have explained the term $\epsilon_{\boldsymbol{k}}\hat{\psi}^\dagger_{\boldsymbol{k}}\hat{\psi}_{\boldsymbol{k}}$, and the term $-2t\gamma_{\boldsymbol{k}}\hat{c}^\dagger_{\boldsymbol{k},\tau}\hat{c}_{\boldsymbol{k},\tau}$ is simply the bare $c1$ electron hopping term written in momentum space. To obtain the second line, we take the Coulomb interaction from our starting Hamiltonian $V_{|\boldsymbol{R}-\boldsymbol{R}'|}\hat{c}^\dagger_{\boldsymbol{R},\tau}\hat{h}^\dagger_{\boldsymbol{R}',\tau'}\hat{h}_{\boldsymbol{R}',\tau'}\hat{c}_{\boldsymbol{R},\tau}$ and use the constraints on the slave particles [Eq. (8)] to express $\sum_{\tau'}\hat{h}^\dagger_{\boldsymbol{R}',\tau'}\hat{h}_{\boldsymbol{R}',\tau'} = 1 + \hat{\psi}^\dagger_{\boldsymbol{R}'}\hat{\psi}_{\boldsymbol{R}'}$. The constant term amounts to a shift of chemical potential (and should be balanced against the background positive charges in any case), thus we ignore it and are left with Eq. (25) in momentum space.

We take the Coulomb interaction to be

$$V(q) = \frac{2\pi e^2}{\epsilon_r}\frac{\tanh(qd)}{q}. \tag{26}$$

The factor $\tanh(qd)$ comes from considering there to be metallic gates at a perpendicular distance d from the TMD bilayer [84,85], which screen the charges at distances greater than d (momenta less than d^{-1}). We set $d \gg a_M$, and have found that our results are insensitive to the precise value. The remaining factors in Eq. (26) are simply the bare interaction for charges forced within a 2D plane.

Although written in second quantization, Eq. (25) in the one-electron and one-holon subspace is a two-body Hamiltonian and can readily be diagonalized numerically. This gives a set of exciton energies $E^X_{n,\boldsymbol{Q}}$ and wave functions $\phi^{(n)}_{\boldsymbol{Q}}(\boldsymbol{p})$, where $\boldsymbol{Q}$ and $\boldsymbol{p}$ are, respectively, the total and relative momenta of the electron-holon pair, and n is a discrete index labeling the eigenstates at given $\boldsymbol{Q}$ (note that the eigenstates are degenerate with respect to the $c1$ electron spin τ). In particular, the energies and wave functions solve the following eigenvalue problem:

$$\sum_{\boldsymbol{q}}\left[\varepsilon_{\boldsymbol{Q}}(\boldsymbol{p})\delta_{\boldsymbol{q},0} - \frac{1}{\mathcal{A}}V(q)\right]\phi^{(n)}_{\boldsymbol{Q}}(\boldsymbol{p}-\boldsymbol{q}) = E^X_{n,\boldsymbol{Q}}\phi^{(n)}_{\boldsymbol{Q}}(\boldsymbol{p}), \tag{27}$$

where $\varepsilon_{\boldsymbol{Q}}(\boldsymbol{p})$ denotes the two-particle kinetic energy

$$\varepsilon_{\boldsymbol{Q}}(\boldsymbol{p}) \equiv \epsilon_{\frac{\boldsymbol{Q}}{2}-\boldsymbol{p}} - 2t\gamma_{\frac{\boldsymbol{Q}}{2}+\boldsymbol{p}}. \tag{28}$$

Equation (27) is the standard Wannier equation for excitons [73], albeit with a modified kinetic energy. Those eigenvalues lying within the band gap correspond to bound states.

To describe normal moiré excitons, we again use Eq. (25) but with bare holes in place of holons. Thus, the term $\epsilon_{\boldsymbol{Q}/2-\boldsymbol{p}}$ in Eq. (28) is replaced by $-2t\gamma_{\boldsymbol{Q}/2-\boldsymbol{p}}$, and we otherwise solve Eq. (27) as before.

With the exciton wave functions in hand, we can define composite boson operators $\hat{X}_{n,\tau}(\boldsymbol{Q})^\dagger$ as in Eq. (3), corresponding to creation of an exciton. Then (in the dilute limit) the Hamiltonian takes the "quadratic" form shown in Eq. (4).

F. Exciton-light coupling

As a final step, we investigate the possibility of optically detecting these excitons via light-matter coupling $\hat{H}_{\text{opt}}$. Within the dipole approximation [73], $\hat{H}_{\text{opt}} \sim \hat{\boldsymbol{j}} \cdot \boldsymbol{A}$, with $\hat{\boldsymbol{j}}$ and $\boldsymbol{A}$ denoting the spatially homogeneous current and vector potential, respectively. We focus on the interband current [86] with the following expression (see Appendix E) as it introduces electron-hole pairs:

$$\hat{\boldsymbol{j}}^{(cv)} = \frac{ev_F}{c} \sum_{\boldsymbol{k},\tau} \boldsymbol{e}_\tau \hat{c}^\dagger_{\boldsymbol{k},\tau} \hat{h}^\dagger_{\boldsymbol{k},\tau} + \text{H.c.}, \tag{29}$$

with polarization vector $\boldsymbol{e}_\tau \equiv \tau \boldsymbol{e}_x - i\boldsymbol{e}_y$. Note that as a result of this polarization vector, circularly polarized light couples selectively to individual spin/valley τ. This is true for both moiré and Mott-moiré excitons [20] since the Hubbard interaction does not enter into the current operator.

To derive further selection rules for Mott-moiré excitons, we rewrite Eq. (29) in terms of the exciton operators $\hat{X}_{n,\tau}(\boldsymbol{Q})^\dagger$ (see Appendix E). For definiteness, we consider photons with the polarization vector of $\boldsymbol{e}_-$, and the corresponding longitudinal optical conductivity obtained from linear response theory is given by [87]

$$\sigma(\omega) \sim \frac{i}{\omega} \sum_n \frac{\left|\Phi^{(n)}_{\boldsymbol{\kappa}}\right|^2}{\omega - E^X_{n,\boldsymbol{\kappa}} + i\delta_+}, \tag{30}$$

where $\Phi^{(n)}_{\boldsymbol{\kappa}} \equiv \frac{1}{\sqrt{N}} \sum_{\boldsymbol{p}} \phi^{(n)}_{\boldsymbol{\kappa}}(\boldsymbol{p})$ is the wave-function amplitude at zero (spatial) separation between electron and holon, specifically at total momentum $\boldsymbol{\kappa}$ in the mBZ (see Fig. 2). δ_+ is an infinitesimal positive regulator. An analogous expression holds for moiré excitons (see Appendix F).

Importantly, since $\sigma(\omega)$ is proportional to the probability of zero separation between charges, *only s-wave excitons are optically bright*. In addition, only the states with $\boldsymbol{Q}$ at mBZ corners contribute to $\sigma(\omega)$. This is because Mott-moiré excitons are electron-*holon* states. Consequently, their total momentum differs from electron-*hole* states by a spin-ordering vector, which is $\boldsymbol{\kappa}$ as indicated by Eq. (11). Hence, our result is consistent with the fact that zero total momentum electron-hole bound states are bright [73].

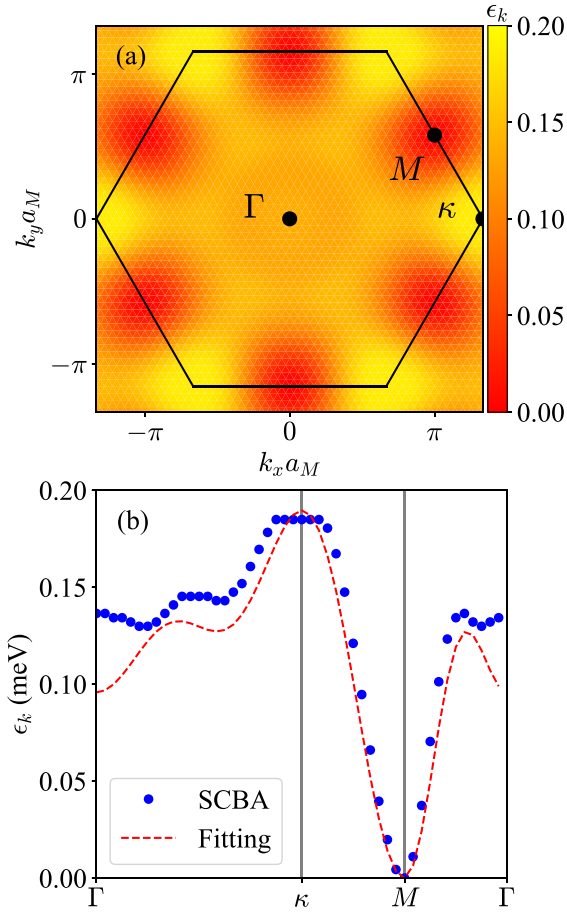

FIG. 8. Dispersion of dressed holon within the SCBA. The moiré period is $a_M = 10$ nm, at which $t \simeq 1.1$ meV and $J \simeq 0.15$ meV according to Ref. [24]. Sublattice magnetization is the equilibrium value $m \simeq 0.48$. System size is 3×24^2 sites. (a) Dispersion ϵ_k throughout the entire mBZ, indicated by the black hexagon. Black dots with labels Γ, κ, and M indicate important mBZ points. (b) Line cut of the dispersion along the path $\Gamma \to \kappa \to M \to \Gamma$. Blue dots give data from the SCBA, and the red dashed line shows the best fit to Eq. (24). The minimum of the dispersion is set arbitrarily to zero.

IV. RESULTS

A. Single holon

We first present results on the properties of individual dressed holons. Although similar results already exist in the literature [47,48], it is useful to review them here for completeness.

In Fig. 8, we show a representative plot of the dressed holon dispersion $\epsilon_{\boldsymbol{k}}$ throughout the mBZ. The minimum is at the point $\boldsymbol{M}$ and the maximum is at the point $\boldsymbol{\kappa}$, both at the edge of the mBZ. We also fit to the dispersion of the effective hopping Hamiltonian in Eq. (23), and find reasonable agreement. The values of the fit parameters $t_{1,2,3}$ as functions of a_M are shown in Fig. 9. Note that, when viewed as functions of t/J (see Appendix A), these results apply to general triangular lattices described by a t-J model and not merely TMD heterobilayers.

The magnitudes of the hopping coefficients decrease significantly as a_M increases. The same is true for the holon

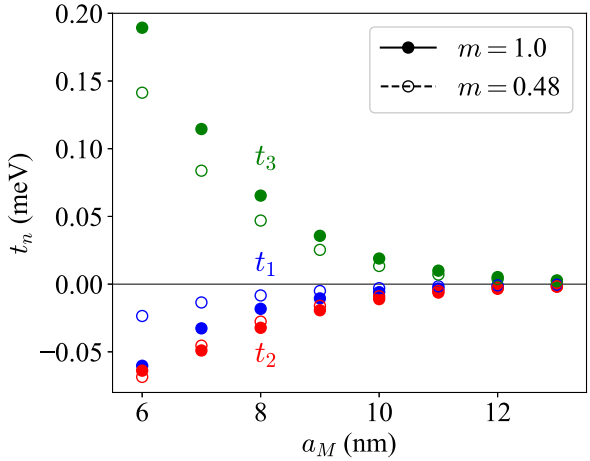

FIG. 9. Fitting parameters $t_{1,2,3}$ of the dressed holon dispersion in Eq. (24) as a function of moiré period a_M. System size is 3×24^2 sites. Solid and empty circles represent data for $m = 1$ and 0.48, respectively. Blue, red, and green denote t_1, t_2, and t_3, respectively.

bandwidth W (see Fig. 4). We find that W is comparable to J, much smaller than the bare hole bandwidth (which scales with t). Qualitatively, this reduction is because a hole in the t-J model is really a magnetic polaron, a charge with a surrounding cloud of spin fluctuations, and the velocity of the polaron is determined by its much slower spin sector [51].

Another perspective on the dressed holon dispersion comes from a Hartree-Fock treatment of the triangular-lattice Hubbard model, which we present in Appendix D. In the large-U limit, the Hartree-Fock Hamiltonian, which amounts to particles hopping in a Zeeman field determined self-consistently from the average magnetization, comes out to be precisely of the form in Eq. (23), with parameters $2t_1 = -t + 3J/2$ and $2t_2 = -2t_3 = -3J/4$. This simple treatment correctly predicts the signs of the effective hoppings, including the extra minus sign in t_1, as well as the locations of band extrema obtained from the more sophisticated SCBA. Interestingly, however, it significantly overestimates the magnitude of the effective hoppings (see Fig. 9), and thus we stick to the SCBA results in what follows.

We lastly compare these properties for $m = 1$ (LSW theory) to $m = 0.48$ (mean-field approximation), also shown in Fig. 9. The magnitudes of $t_{1,2,3}$ are all reduced for the smaller magnetization, but otherwise the behavior is largely unaffected.

B. Mott-moiré exciton

We now turn to the properties of Mott-moiré excitons obtained by solving Eq. (27). We compare these results to those of normal moiré excitons, where strong correlations in the $v1$ band play no role. All numerical data use dielectric constant $\epsilon_r = 10$ unless otherwise noted.

1. Exciton dispersion

First, we discuss the dispersion profile for the lowest-energy moiré and Mott-moiré excitons (see Figs. 2 and 10). The former has a minimum at Γ and a maximum at κ, whereas the latter has a maximum at Γ and a minimum at M.

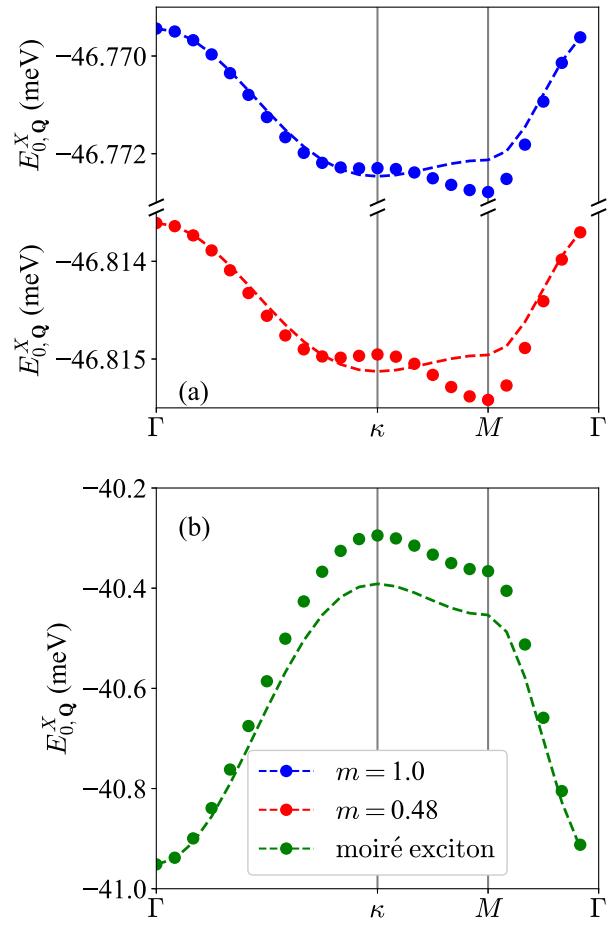

FIG. 10. Center-of-mass dispersion for the lowest-energy exciton $E^X_{0,Q}$, along the path $\Gamma \to \kappa \to M \to \Gamma$ (see Fig. 2). Moiré period is $a_M = 10$ nm, dielectric constant is $\epsilon_r = 10$, and system size is 3×24^2 sites. (a) Numerical results for Mott-moiré excitons at $m = 1$ (blue circles) and $m = 0.48$ (red circles). Dashed lines denote dispersions obtained from perturbation theory, Eq. (G6) (shifted so as to coincide with data at the Γ point). (b) Numerical results for moiré excitons. Dashed line again denotes the prediction from perturbation theory, Eq. (G2).

Furthermore, the bandwidth of Mott-moiré excitons is drastically narrower than that of moiré excitons.

We can understand these differences by noting that at large superlattice period a_M, since the kinetic energy scale decreases exponentially with a_M but the interaction scale decreases only as $1/a_M$, the term $\varepsilon_{\boldsymbol{Q}}(\boldsymbol{p})$ in Eq. (27) can be treated as a perturbation compared to $V(q)$. At zeroth order, the exciton eigenstates are simply (relative) position eigenstates since these diagonalize the Coulomb interaction. Denote the unperturbed eigenstates by $|j, \boldsymbol{Q}\rangle$, with j an integer labeling positions in order of increasing separation, and denote the unperturbed energies by $-V_j$. We give details of the perturbation theory in Appendix G, ultimately finding that the first momentum-dependent correction to the moiré exciton is $-\frac{t^2}{V_0-V_1}\gamma_{\boldsymbol{Q}}$ whereas that for the Mott-moiré exciton is $\frac{t|t_1|}{V_0-V_1}\gamma_{\boldsymbol{Q}}$ (the factor of t comes from the electron hopping and the factor of t_1 from the holon). Note first of all the relative minus sign between the two, and second that the Mott-moiré dispersion is

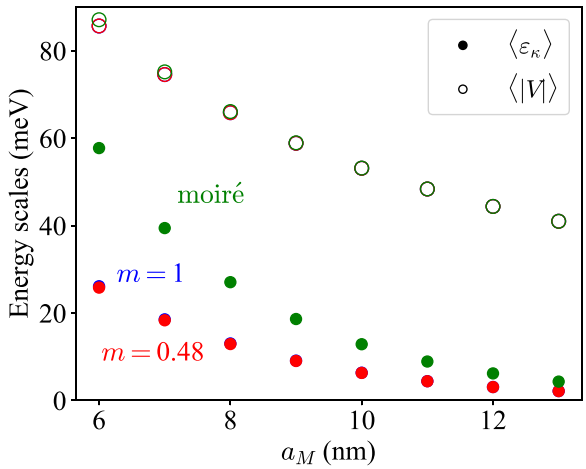

FIG. 11. Average kinetic and potential energies for the lowest-energy exciton as a function of moiré period a_M. Total momentum is set to $\boldsymbol{Q} = \boldsymbol{\kappa}$. Dielectric constant is $\epsilon_r = 10$, and system size is 3×24^2 sites. Blue and red circles are data for Mott-moiré excitons at $m = 1$ and 0.48, respectively (indistinguishable at this scale). Green circles are for moiré excitons. Solid markers indicate the two-particle kinetic energy $\langle \varepsilon_\kappa \rangle$ [Eq. (28)], and empty markers indicate the Coulomb energy $\mathcal{A}^{-1}\langle |V(q)| \rangle$ [Eq. (26) with $\mathcal{A}$ the system area].

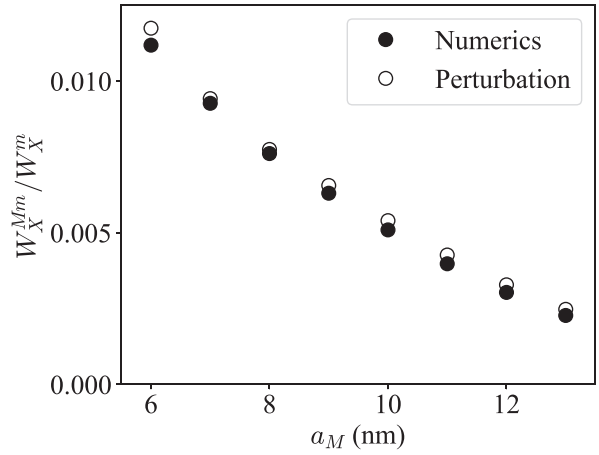

FIG. 12. Ratio between the bandwidths of Mott-moiré (W_X^{Mm}) and moiré (W_X^m) excitons from data (solid circles, see also Fig. 3) and from Eq. (G7) (empty circles).

reduced by an overall factor of $|t_1|/t$. Thus, we see that both the inverted dispersion and smaller bandwidth of Mott-moiré excitons can be traced back to the renormalization of the holon hopping.

Recall that the extra minus sign in t_1, and thus the inverted Mott-moiré dispersion, can be understood through Hartree-Fock theory, which treats the background spin order as static. Spin *fluctuations* can therefore be seen as not essential to this phenomenon. However, they play a much more significant role in the reduced Mott-moiré bandwidth since Hartree-Fock theory alone overestimates the magnitude of t_1, and thus the bandwidth, significantly as compared to the SCBA.

2. Properties of the lowest exciton state

We now turn to detailed properties of the lowest-energy excitons, particularly their binding energies, sizes, and bandwidths. The results are summarized in Fig. 3.

Figure 11 compares the separate kinetic and potential energies of both excitons. As argued above, the potential energy is noticeably larger than the kinetic energy within the range of a_M we consider, especially for Mott-moiré excitons. This both explains the small exciton diameters $\langle r \rangle_X \ll a_M$ [see Fig. 3(b)] and justifies our perturbative treatment outlined in Appendix G.

Since the Coulomb attraction conserves the total momentum $\boldsymbol{Q}$, we define the binding energy as $E^B_{0,\boldsymbol{Q}} \equiv \min_{\boldsymbol{p}} \varepsilon_{\boldsymbol{Q}}(\boldsymbol{p}) - E^X_{0,\boldsymbol{Q}}$, i.e., the difference between $E^X_{0,\boldsymbol{Q}}$ and the lowest noninteracting two-particle state at momentum $\boldsymbol{Q}$. The perturbative analysis described above gives $E^B_{0,\boldsymbol{Q}} \sim V_0 - 6t - 2t\gamma_{\boldsymbol{Q}}$ for moiré excitons and $E^B_{0,\boldsymbol{Q}} \sim V_0 - 6t$ for Mott-moiré excitons. This explains the slightly larger binding energy for moiré excitons at $\boldsymbol{Q} = \boldsymbol{\kappa}$ [see Fig. 3(a)]. We refer to Appendix G for more details.

Finally, we elaborate on the bandwidth W_X for both excitons. We have already discussed how the significantly smaller Mott-moiré bandwidth is a consequence of the dressed holon dispersion, but our perturbative analysis makes a further quantitative prediction: the reduction of the bandwidth is $|t_1/t|$ to leading order. We show in Fig. 12 that this result is borne out quite well in the numerics. A further observation is that even the moiré bandwidth itself is much smaller than the hopping coefficient t which one might naively expect. This effect is due to strong Coulomb binding on the lattice [88], with physical origin given above.

3. Excited states and optical spectrum

The first few excited-state exciton energies $E^X_{n,\boldsymbol{Q}}$ are shown in Fig. 13(a), at the values of $\boldsymbol{Q}$ relevant for the optical conductivity in both cases (Γ for moiré and κ for Mott-moiré). These levels are not well described by the Rydberg series $E^X_{n,\boldsymbol{Q}} \sim (2n+1)^{-1}$ found in hydrogenic excitons [73], but this is merely a consequence of the lattice structure together with the small exciton radii. Also note that our use of a two-band model restricts us to excitonic states formed from the valence and conduction moiré bands, whereas experimental optical spectra would include contributions from composite particles having constituents in other moiré bands.

Figure 13(b) plots the wave-function amplitude $\Phi^{(n)}_{\boldsymbol{Q}}$ which determines the oscillator strength. The lowest-energy states substantially dominate the spectra (for both excitons) and, furthermore, as discussed in Sec. III, only s-wave excitons exhibit a response.

4. Exciton wave function

We show the lowest state wave functions of different angular momentum (s, p, d, or f symmetry) for Mott-moiré exciton at $\boldsymbol{Q} = \boldsymbol{\kappa}$ in Fig. 14. We understand their rotational properties with the $D3$ point-group symmetry of Eq. (27) (in terms of the electron momentum $\boldsymbol{p}_e = \frac{\boldsymbol{\kappa}}{2} - \boldsymbol{p}$). $D3$ point group should give two one-dimensional representations and one two-dimensional representation [89]. The one-dimensional representations can be identified as s- and f-wave states

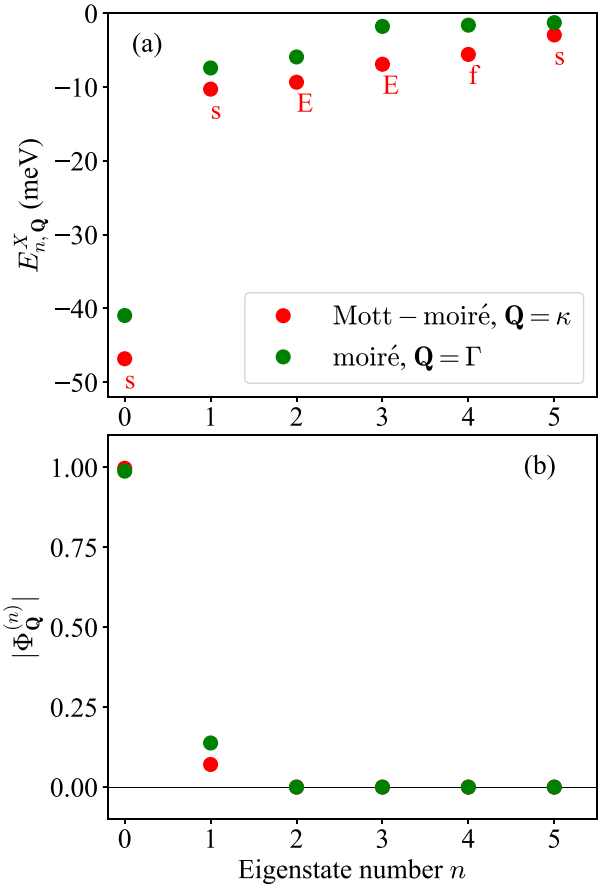

FIG. 13. (a) Energies $E^X_{n,\boldsymbol{Q}}$ of the first few excited states for moiré and Mott-moiré excitons, at the indicated total momenta. The labels s, E, and f denote the $D3$ group representations with which the states are associated. (b) Wave-function amplitude $|\Phi^{(n)}_{\boldsymbol{Q}}|$ which determines the oscillator strength, for the first few excited states of both excitons. The eigenstate number n simply labels the states (only one of each degenerate pair is shown). The total momenta used ($\boldsymbol{Q} = \boldsymbol{\kappa}$ for Mott-moiré and $\boldsymbol{Q} = \boldsymbol{\Gamma}$ for moiré) are those which are relevant for the optical conductivity [see Eqs. (30) and (F4)]. Data are for moiré period $a_M = 10$ nm, dielectric constant $\epsilon_r = 10$, magnetization $m = 0.48$, and system size 3×24^2 sites.

(see Fig. 14). The two-dimensional representation, which we label E, cannot be interpreted cleanly in terms of the usual angular momentum classification (Fig. 14 shows examples of apparently p- and d-wave states which both belong to E).

C. Spectator exciton

We end the results with spectator excitons, providing an additional signature of spin correlation in the half-filled $v1$ band. These excitations are the lowest internal bound states between a hole in some valence moiré band other than $v1$, say $v2$ (with annihilator $\hat{v}$), and a conduction electron (assumed to be $c1$ for simplicity). Note that neither band involved is directly subject to strong-correlation physics. Nonetheless, the composite particles could gain $v1$-spin information via the exchange interaction [5,62,64] between $v1$ and $v2$ bands (see Fig. 15). Specifically, this vertex could flip $v2$ spins upon scattering with $v1$, introducing coupling between

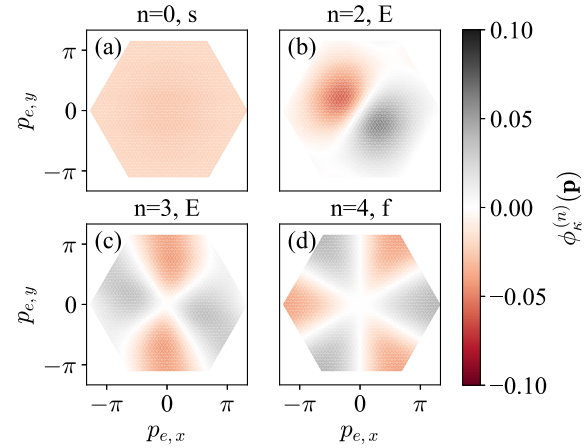

FIG. 14. The wave functions for the first few excited states of Mott-moiré excitons. We set the total momenta $\boldsymbol{Q} = \boldsymbol{\kappa}$, the moiré period $a_M = 10$ nm, and the magnetization $m = 0.48$ for this figure. The axes $(p_{e,x}, p_{e,y})$ denote the $c1$ electron momentum of the exciton, within the first mBZ. The color bar gives the exciton wave function $\phi^{(n)}_{\kappa}(\boldsymbol{p})$. n in the titles denote the eigenstate number in Fig. 13 to which the wave functions belong. The $n = 0$ and 1 states are s waves with different energies. The $n = 1$ state is similar to $n = 0$ and is not plotted here. The p-wave-like state $n = 2$ and d-wave-like state $n = 3$ are doubly degenerate. The $n = 4$ state is f wave. The s, E, and f labels in the titles denote the $D3$ group representations with which the states are associated.

the excitons $\hat{x}_\tau = \hat{v}_\tau \hat{c}_\tau$ and $\hat{y}_\tau = \hat{v}_{-\tau}\hat{c}_\tau$. Such a scattering process is present with a 120° coplanar spin order, opening a gap Δ_{xy} between the two spectator excitons. We find that Δ_{xy} is proportional to the sublattice magnetization m in $v1$ (see Appendix I). Crucially, the two excitons are degenerate when $v1$ is magnetically disordered, giving a qualitative distinction between the presence and absence of spin order.

We estimate the gap (see Fig. 16) by taking $v2$ to be the next valence moiré orbital centered around the same set of

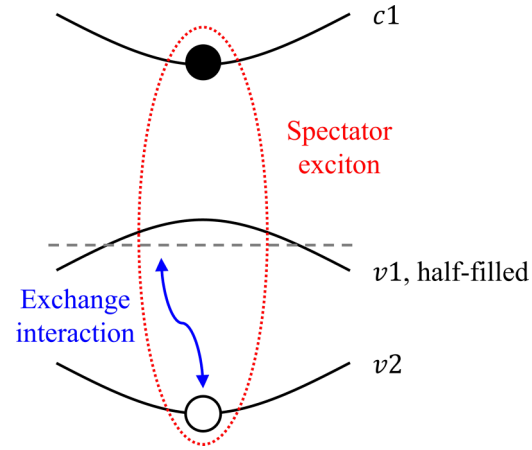

FIG. 15. Illustration of the spectator exciton formed by an electron in $c1$ band and a hole in $v2$ band. It couples to the spin states in the half-filled (denoted with gray dashed line) $v1$ band via exchange interaction.

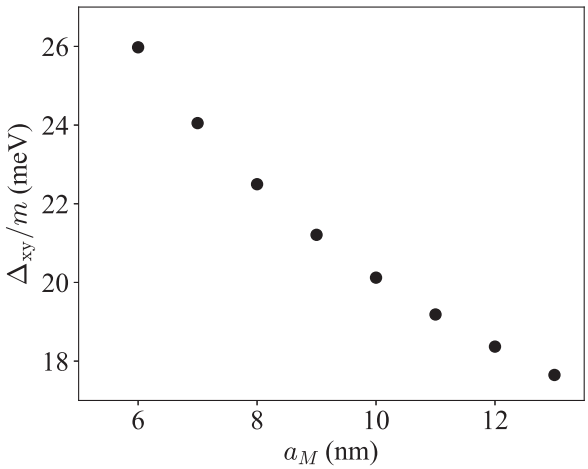

FIG. 16. The spectator exciton gap Δ_{xy} divided by the sublattice magnetization m of 120° coplanar spin order as a function of moiré period a_M. Numerical calculation follows Eq. (I13) using moiré potential parameters taken from Ref. [24] for WSe_2 on top of $MoSe_2$ and dielectric constant $\epsilon_r = 10$ (see Appendix I for more details).

lattice sites as $v1$. Δ_{xy} decreases with a larger moiré period due to suppressed exchange matrix elements from more extended Wannier orbitals [see Eq. (I13)]. In addition, we find $\Delta_{xy} \simeq 20$ meV at full magnetization: note that this quantitative value depends on the microscopic details, such as the approximate orbitals. The fact that Δ_{xy} is much larger than the superexchange constant J may imply that the exciton dynamics has a significant back-reaction on the spin correlations, which is beyond our analysis. Nevertheless, we still anticipate that the spin-induced spectator exciton gap would be rather large. We refer to Appendix I for details.

We end by pointing out other variants of spectator excitons. These include bound states with charges in moiré bands other than $c1$, $v1$, and $v2$. More generally, they could even be outside of the moiré bilayer [33]; as long as they couple to $v1$ spin states with exchange interaction, the same physics is present and the splitting Δ_{xy} indicates whether there is spin correlation.

V. CONCLUSION

We have demonstrated the existence of bound states between spin-dressed holons, i.e., magnetic polarons, and conduction electrons on the moiré superlattice of twisted TMD heterobilayers. Such bound states, named Mott-moiré excitons, possess much narrower bandwidths than moiré excitons. Thus, the degree of correlations, controllable by gate voltages [84,85], offers a further mechanism to engineer exciton properties. This is in addition to the already high tunability provided by the moiré period. However, we predict that only *s*-wave excitons (both moiré and Mott-moiré) are detectable via optical measurements.

These results are a consequence of two simple physical features. First, the kinetic energy of the holon is heavily suppressed by spin fluctuations. We further draw a distinction between effects which are due to the presence of *static* spin order versus genuine *fluctuations*: inversion of the Mott-moiré dispersion can be traced to the former, but the reduction of the bandwidth is due to the latter. Second, the Coulomb energy is much larger than kinetic at large moiré periods due to the exponential suppression of the latter. This allows us to treat the hopping terms as a perturbation, and the exciton properties follow straightforwardly.

One natural question is how to distinguish between moiré and Mott-moiré excitons experimentally. Since the main difference is in their masses (i.e., bandwidths), we propose diffusion measurements as one viable possibility. Intuitively, excitons with larger mass should have slower diffusion, and so diffusion constants should be significantly reduced in the presence of magnetic polaron physics. Recent diffusion measurements have been performed on excitons in TMD heterobilayers [39–41], but have not compared different fillings of the $v1$ band (and hence degree of correlations) to the best of our knowledge.

Aside from Mott-moiré excitons, we also study spectator excitons, bound states between charges outside of the strongly correlated moiré band. Incorporating the exchange interaction, we find that they exhibit additional energy splitting when the correlated band is 120° spin ordered. This result, together with the modified mass of Mott-moiré excitons, demonstrates the importance of spin physics for optical excitations in TMDs.

Nevertheless, the existing experiments have focused thus far on effects due to charge order [31–33,36] rather than spin correlation. Since the energy scale for charge order is U and that for spin correlation is only J, it should be possible to separate these effects by varying the temperature T. Changes at $T \sim J$ can likely be attributed to spin physics alone. One example is the exchange-induced splitting of spectator excitons [90]. Another is the enhancement of the Mott-moiré exciton mass, which should appear once the spin correlation length exceeds the polaron size. These qualitative differences at distinct temperature regimes could provide signatures for spin correlation, and our work gives two platforms for corresponding measurements. We therefore expect that our systematic study on these strongly correlated bound states can inform these future experiments.

Much work regarding Mott excitons remains to be done beyond the interband species considered here. For example, at half-filling of the $v1$ band, there should also exist *intraband* excitons consisting of two magnetic polarons [see Fig. 1(b)]. Previous work has discussed these excitons for a single-band Hubbard model on the square lattice [44], but no such work for triangular moiré superlattices has been done to the best of our knowledge. The optical properties of strongly correlated excitons, both interband and intraband, such as their coupling to optical cavities and potential cavity-QED effects, are also highly active topics [91,92].

Moreover, twisted TMD bilayers show various strong-correlation phases besides 120° antiferromagnetic insulators, and excitons therein remain unexplored. For instance, systems allowing for a next-nearest-neighbor superexchange could give rise to spin liquids in a half-filled $v1$ band [24,27]. Another example at the same filling is the charge-transfer insulator [30,93] in which Hubbard U is larger than the gap between the first two valence moiré bands [94]. In addition, other charge and spin orders emerge at fractional

fillings of the $v1$ band, such as Wigner crystal and ferromagnetism [24,27]. The properties of excitons and whether they are relevant optical excitations in these correlated phases remain open.

Finally, another field to be investigated is the *multi*exciton many-body physics in moiré TMDs. Beyond the dilute-exciton limit, these composite particles could significantly alter the strong correlations. This is crucial for understanding excitonic insulators in TMD multilayer heterostructures [95,96]. Nonetheless, the interplay between exciton occupation and correlated insulating phases is still an open question.

ACKNOWLEDGMENTS

T.-S.H. thanks D. Suarez Forero, S. Sarkar, and B. Gao for beneficial experimental discussions. Y.-Z.C. thanks Z. Wang for discussions related to slave particles. M.H. thanks A. Imamoglu and A. Srivastava for extensive fruitful discussions. The work at Maryland was supported by JQI-NSF-PFC, Laboratory for Physical Sciences, QLCI Grants No. OMA-2120757, No. ARO W911NF2010232, No. AFOSR FA9550-19-1-0399, and No. FA95502010223, and Minta Martin and Simons Foundation. F.W. is supported by the National Key Research and Development Program of China Grant No. 2021YFA1401300 and start-up funding of Wuhan University.

APPENDIX A: RESULTS IN DIMENSIONLESS VARIABLES

Our results apply to generic triangular lattices beyond moiré TMDs to which the two-band model (2) applies. t and U (or J) are sufficient to set the dressed holon properties in $v1$ band. For moiré TMDs, these energy scales are dependent on the moiré period a_M (see Fig. 17). We accordingly present the holon results as functions of the t/J (instead of a_M in Figs. 18 and 19) so that the results can be generalized to generic triangular lattices. Similarly, we show how the exciton properties evolve with t/J in Fig. 20. Note that here we fix the Coulomb energy scale V_1 while varying t/J (whereas all energy scales change with a_M for moiré TMDs.)

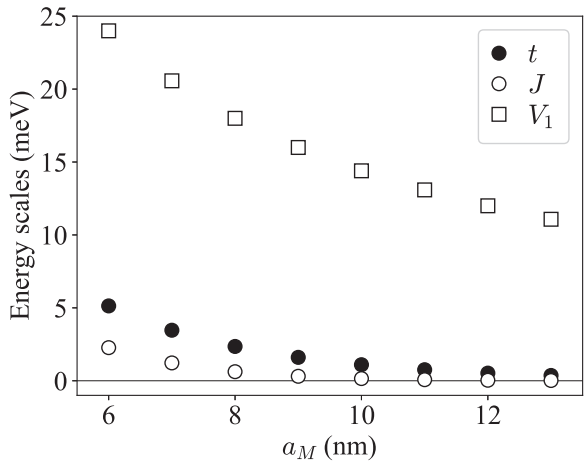

FIG. 17. Energy scales t (solid circles) and J (empty circles) for the t-J model in Eq. (5) as a function of moiré period a_M, taken from Ref. [24] for WSe_2 on top of $MoSe_2$. Also shown are the nearest-neighbor Coulomb scale $V_1 = \frac{e^2}{\epsilon_r a_M}$ (empty squares), using dielectric constant $\epsilon_r = 10$.

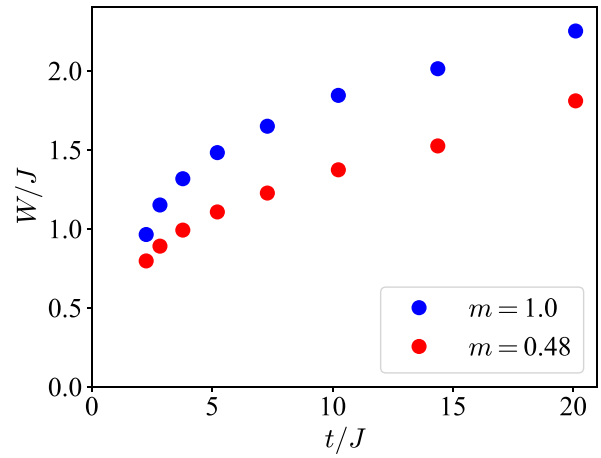

FIG. 18. Dressed holon bandwidth W (in units of J) from SCBA as a function of t/J (values taken from Fig. 17), at different sublattice magnetizations m (blue and red). System size is 3×24^2 sites.

APPENDIX B: SLAVE-FERMION t-J MODEL IN THE HOLSTEIN-PRIMAKOFF REPRESENTATION FOR SPIN

In this Appendix, we provide the details of Holstein-Primakoff (HP) representation of the slave-fermion t-J model Eqs. (9) and (10). Following Eq. (12), we express the spinon operator in terms of HP bosons as follows:

$$\hat{s}_{\boldsymbol{R},\tau} = \frac{1}{\sqrt{2}} e^{i\tau\frac{2\pi\theta_{\boldsymbol{R}}}{3}} \left(\sqrt{2S - \hat{a}^\dagger_{\boldsymbol{R}}\hat{a}_{\boldsymbol{R}}} - \tau\hat{a}_{\boldsymbol{R}}\right), \tag{B1}$$

where $\theta_{\boldsymbol{R}} = 0, -1, 1$ for A, B, and C sublattices, respectively, and S is the magnitude of spin ($S = \frac{1}{2}$ in our problem). To simplify the problem and incorporate the depletion of magnetization by quantum fluctuation, we employ a mean-field approximation: $\hat{a}^\dagger_{\boldsymbol{R}}\hat{a}_{\boldsymbol{R}}$ in Eq. (B1) is replaced by $\frac{1}{N}\sum_{\boldsymbol{R}}\langle\hat{a}^\dagger_{\boldsymbol{R}}\hat{a}_{\boldsymbol{R}}\rangle$,

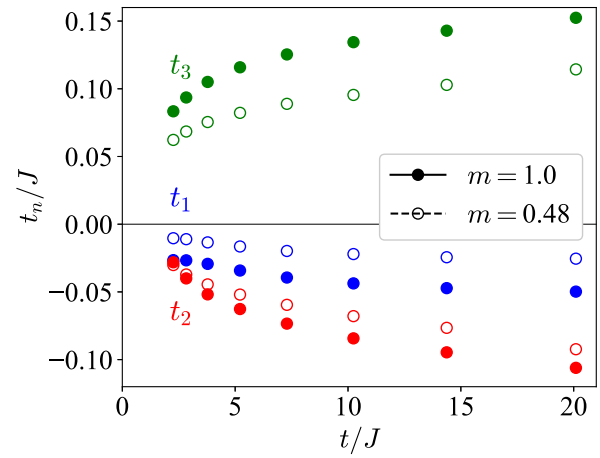

FIG. 19. Fitting parameters $t_{1,2,3}$ of the dressed holon dispersion (in units of J) in Eq. (24) as a function of t/J (values taken from Fig. 17). System size is 3×24^2 sites. Solid and empty circles represent data for $m = 1$ and 0.48, respectively. Blue, red, and green denote t_1, t_2, and t_3, respectively.

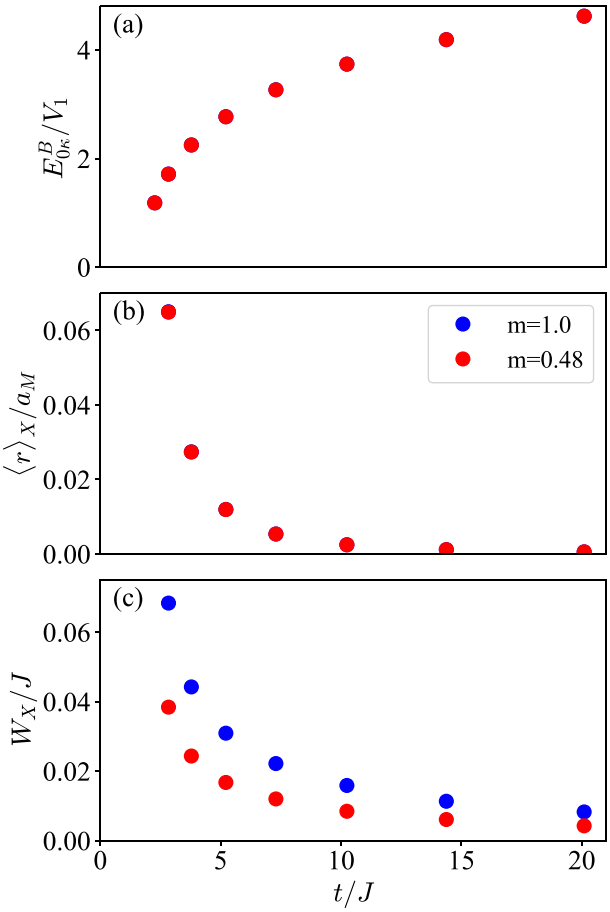

FIG. 20. Properties of Mott-moiré excitons at different magnetization (blue and red, indistinguishable at the scales of top and middle panels) as functions of the moiré period a_M. Dielectric constant is $\epsilon_r = 10$. System size is $N = 3\times 24^2$ sites. (a) Binding energy of the lowest internal state $E^B_{0,\kappa}$ at total momentum $\boldsymbol{Q} = \boldsymbol{\kappa}$, which has the largest binding among all $\boldsymbol{Q}$. Energies are in units of $V_1 \equiv \frac{e^2}{\epsilon_r a_M}$, where we fix $a_M = 10$ nm while varying t/J. (b) Average diameter of excitons at total momentum κ, in units of a_M. (c) Exciton bandwidths W_X, in units of J. Values for t and J as functions of a_M are taken from Ref. [24] for WSe_2 on top of $MoSe_2$ (see also Fig. 17).

where the expectation value is taken with respect to the mean-field ground state of Eq. (10). This leads to

$$\hat{s}_{\boldsymbol{R},\tau} \to \frac{1}{\sqrt{2}} e^{i\tau\frac{2\pi\theta_{\boldsymbol{R}}}{3}}(\xi - \tau\hat{a}_{\boldsymbol{R}}), \tag{B2}$$

where $\xi = \sqrt{(1+m)/2}$ and m is the sublattice magnetization in the HP representation:

$$m = 1 - \frac{2}{N}\sum_{\boldsymbol{R}}\langle\hat{a}^\dagger_{\boldsymbol{R}}\hat{a}_{\boldsymbol{R}}\rangle. \tag{B3}$$

As a consequence of the transformation, the slave-particle constraint (8) in the dilute charge limit, i.e., setting the holon occupation to zero, within the mean-field approximation is expressed as

$$\xi^2 + \hat{a}^\dagger_{\boldsymbol{R}}\hat{a}_{\boldsymbol{R}} = 1, \tag{B4}$$

and averaging out all moiré sites $\boldsymbol{R}$, it becomes

$$\xi^2 + \frac{1}{N}\sum_{\boldsymbol{q}}\langle\hat{a}^\dagger_{\boldsymbol{q}}\hat{a}_{\boldsymbol{q}}\rangle = 1. \tag{B5}$$

The slave-fermion t-J model in the HP representation within the mean-field approximation is derived as

$$\begin{aligned}
\hat{H}_{tJ} &\approx \hat{H}_t + \hat{H}_J,\\
\hat{H}_t &= \left(\frac{t\xi}{2}\right)\sum_{\langle\boldsymbol{R},\boldsymbol{R}'\rangle}[\xi + \sqrt{3}\epsilon_{\boldsymbol{R}\boldsymbol{R}'}\hat{a}_{\boldsymbol{R}}]\hat{\psi}^\dagger_{\boldsymbol{R}}\hat{\psi}_{\boldsymbol{R}'} + \text{H.c.},\\
\hat{H}_J &= \bar{\lambda}\sum_{\boldsymbol{R}}\hat{a}^\dagger_{\boldsymbol{R}}\hat{a}_{\boldsymbol{R}}\\
&\quad + \left(\frac{J\xi^2}{8}\right)\sum_{\langle\boldsymbol{R},\boldsymbol{R}'\rangle}[\hat{a}^\dagger_{\boldsymbol{R}}\hat{a}_{\boldsymbol{R}'} - 3\hat{a}^\dagger_{\boldsymbol{R}}\hat{a}^\dagger_{\boldsymbol{R}'} + \text{H.c.}],
\end{aligned} \tag{B6}$$

where $\epsilon_{\boldsymbol{R}\boldsymbol{R}'}$ is the Levi-Civita symbol which is antisymmetric, i.e., $\epsilon_{\boldsymbol{R}\boldsymbol{R}'} = -\epsilon_{\boldsymbol{R}'\boldsymbol{R}}$, and depends only on $\theta_{\boldsymbol{R}}$, the sublattice label of $\boldsymbol{R}$. Explicitly, $\epsilon_{AB} = \epsilon_{BC} = \epsilon_{CA} = 1$ and $\epsilon_{BA} = \epsilon_{CB} = \epsilon_{AC} = -1$. The constraint in Eq. (B5) can be incorporated through a Lagrangian multiplier $\bar{\lambda}$, which takes the value of $3J\xi^2/2$, determined by minimizing $\langle\hat{H}_J\rangle$. Also, $\bar{\lambda} = 3J\xi^2/2$ gives gapless spin-wave excitations, consistent with the Goldstone mode from spontaneous symmetry breaking of continuous symmetry. We also ignore the processes involving more than one HP boson, e.g., $\hat{\psi}^\dagger\hat{\psi}\hat{a}^\dagger\hat{a}$ and $\hat{a}^\dagger\hat{a}^\dagger\hat{a}\hat{a}$, since we are interested in the magnetic ordered state. In the main text, Eqs. (19) and (14) are derived with a Bogoliubov rotation $\hat{\beta}_{\boldsymbol{q}} = u_{\boldsymbol{q}}\hat{a}_{\boldsymbol{q}} - v_{\boldsymbol{q}}\hat{a}^\dagger_{-\boldsymbol{q}}$, where u_q and v_q are defined in Eqs. (17) and (18), respectively.

To determine the equilibrium magnetization self-consistently, we apply the Bogoliubov rotation to Eq. (B5), giving

$$\begin{aligned}
\xi^2 &= 1 - \frac{1}{N}\sum_{\boldsymbol{q}} v^2_{\boldsymbol{q}},\\
m &= 1 - \frac{2}{N}\sum_{\boldsymbol{q}} v^2_{\boldsymbol{q}}.
\end{aligned} \tag{B7}$$

We calculate the equilibrium magnetization by numerically doing the sum on the right-hand side of Eq. (B7) for system size as large as possible. Here we do such calculation for system with size $N = 3L^2$ for $L = 500, 1000, \ldots, 3000$, following with an extrapolation using a linear fitting between m and L^{-1}. It turns out that at $L \to \infty$, the result obtained is $m \simeq 0.478\,96$. Hence, in our calculation we take $m = 0.48$ as the equilibrium magnetization, which is close to the value reported in literature [78].

APPENDIX C: NUMERICAL SOLUTION OF THE DRESSED HOLON DISPERSION WITHIN SCBA

In this Appendix, we discuss the numerical procedures for solving SCBA. To numerically solve Eq. (22), we use the fact that all $\omega_{\boldsymbol{q}}$ are non-negative. We also exclude the momenta with $\omega_{\boldsymbol{q}} = 0$ since the corresponding states do not belong to spin excitation. Therefore, from Eq. (22), we find that $\Sigma_{\boldsymbol{k}}(\epsilon)$ can be always expressed in terms of $\Sigma_{\boldsymbol{k}}(\epsilon')$ with $\epsilon' < \epsilon$. With

a sufficiently negative ϵ we can approximate the dressed holon self-energy as

$$\Sigma_{\boldsymbol{k}}(\epsilon) \approx \frac{3t^2\xi^2}{N}\sum_{\boldsymbol{q}}\frac{M^2_{\boldsymbol{k},\boldsymbol{q}}}{\epsilon-\omega_{\boldsymbol{q}}-t\xi^2\gamma_{\boldsymbol{k}+\boldsymbol{q}}}. \tag{C1}$$

For numerical implementation, we pick an $\epsilon' < 0$ that is large enough in magnitude such that $\Sigma_{\boldsymbol{k}}(\epsilon')$ satisfies Eq. (C1). Denoting small increment in ϵ as $\Delta\epsilon$, $\Sigma_{\boldsymbol{k}}(\epsilon'+\Delta\epsilon)$ is determined by $\Sigma_{\boldsymbol{k}}(\epsilon')$ according to Eq. (22). Hence, for $\epsilon-\epsilon'$ being multiples of $\Delta\epsilon$, we can generate $\Sigma_{\boldsymbol{k}}(\epsilon)$ recursively.

The dressed holon dispersion is determined by the pole of the dressed holon propagator $G_{\boldsymbol{k}}(\epsilon)$, which is given by

$$G_{\boldsymbol{k}}(\epsilon) = \frac{1}{\epsilon - t\xi^2\gamma_{\boldsymbol{k}} - \Sigma_{\boldsymbol{k}}(\epsilon) + i0_+}, \tag{C2}$$

where the infinitesimal regulator 0_+ is added as $(0.1t)$ to implement the numerical calculation. Hence, the dressed holon dispersion can be obtained by numerically solving $\epsilon_{\boldsymbol{k}} = \Sigma_{\boldsymbol{k}}(\epsilon_{\boldsymbol{k}}) + t\xi^2\gamma_{\boldsymbol{k}}$.

A potential issue in numerically solving the self-consistent equations is that there might be mulitple solutions, and it is not guaranteed that the solution obtained in this way is the one of interest, which is the lowest energy one. Here we alternatively solve for the dressed holon dispersion by finding the lowest-energy peak of the spectral function $-\frac{1}{\pi}\mathrm{Im}G_{\boldsymbol{k}}(\epsilon)$.

APPENDIX D: HARTREE-FOCK ANALYSIS OF THE HOLE DISPERSION IN TRIANGULAR-LATTICE HUBBARD MODEL

In this Appendix, we provide an alternative analysis to the hole dispersion for the triangular-lattice Hubbard model from Eq. (2). We begin by considering a Hartree-Fock trial Hamiltonian including the hopping term of the Hubbard model and a sublattice Zeeman splitting field:

$$\begin{aligned}\hat{H}_0 &= \hat{H}_t + \hat{H}_Z,\\ \hat{H}_Z &= -h_Z\sum_{\tau,\tau'}\sum_{\boldsymbol{R}}\hat{h}_{\boldsymbol{R},\tau}(\hat{\boldsymbol{\sigma}}_{\tau\tau'}\cdot\hat{\boldsymbol{n}}_{\boldsymbol{R}})\hat{h}^\dagger_{\boldsymbol{R},\tau'},\end{aligned} \tag{D1}$$

where $\hat{\boldsymbol{n}}_{\boldsymbol{R}}$ are sublattice unit vectors defined in Eq. (11), and h_Z is the variational parameter characterizing the strength of the sublattice Zeeman field in the trial Hamiltonian. We use this Zeeman field term to capture the effect of 120° spin order from the triangular lattice Hubbard model. Note that this trial Hamiltonian is quadratic in fermion while the original Hubbard Hamiltonian is interacting.

Next, we obtain a trial density matrix $\hat{\rho}_0 = Z_0^{-1}e^{-\frac{\hat{H}_0}{T}}$ from this trial Hamiltonian $\hat{H}_0$:

$$F[h_Z] = \langle\hat{H}-\hat{H}_0\rangle_{\hat{\rho}_0} + F_0[h_Z], \tag{D2}$$

where we write the entropy term of the free energy as $T\langle\log\hat{\rho}_0\rangle_{\hat{\rho}_0} = F_0[h_Z] - \langle\hat{H}_0\rangle_{\hat{\rho}_0}$. To determine $\hat{\rho}_0$, and hence h_Z, we minimize the free energy with respect to the variational parameter h_Z, giving

$$\partial_{h_Z}\langle\hat{H}_U-\hat{H}_Z\rangle_{\hat{\rho}} = -\partial_{h_Z}F_0[\hat{\rho}], \tag{D3}$$

in which we set $\hat{H}$ to be the triangular-lattice Hubbard model in Eq. (2), with the onsite repulsion denoted as $\hat{H}_U$. The expectation value $\langle\hat{H}_U\rangle$ is derived as

$$\langle\hat{H}_U\rangle_{\hat{\rho}_0} = \frac{NU}{3}\sum_{\theta_{\boldsymbol{R}}}\frac{1-\boldsymbol{m}(\theta_{\boldsymbol{R}})^2}{4}, \tag{D4}$$

where $\theta_{\boldsymbol{R}} \in \{0, 1, -1\}$ labels the sublattice of moiré site $\boldsymbol{R}$, as defined in Appendix B, and $\boldsymbol{m}(\theta_{\boldsymbol{R}})$ denotes the Hartree-Fock sublattice order parameter, which is expressed as

$$\boldsymbol{m}(\theta_{\boldsymbol{R}}) = \frac{3}{N}\sum_{\tau,\tau'}\sum_{\boldsymbol{R}\in\theta_{\boldsymbol{R}}}\hat{\boldsymbol{\sigma}}_{\tau\tau'}\langle\hat{h}_{\boldsymbol{R},\tau}\hat{h}^\dagger_{\boldsymbol{R},\tau'}\rangle_{\hat{\rho}_0}. \tag{D5}$$

With these expressions, we reduce Eq. (D3) to

$$h_Z\hat{\boldsymbol{n}}_{\boldsymbol{R}} = \frac{U}{2}\boldsymbol{m}(\theta_{\boldsymbol{R}}). \tag{D6}$$

To continue, we need to diagonalize the trial Hamiltonian $\hat{H}_0$. The convenient way to do this is to apply a spin rotation $\hat{U}_{\boldsymbol{R}}$ from $\boldsymbol{e}_z$ to $\hat{\boldsymbol{n}}_{\boldsymbol{R}}$, which is defined previously in Eq. (12), and define the rotated fermion operator $\hat{\tilde{h}}^\dagger_{\boldsymbol{R},\tilde{\tau}} = \sum_\tau[\hat{U}_{\boldsymbol{R}}]_{\tilde{\tau},\tau}\hat{h}^\dagger_{\boldsymbol{R},\tau}$, where $\tilde{\tau} = \{+,-\}$ labels the spin state aligned and antialigned to $\hat{\boldsymbol{n}}_{\boldsymbol{R}}$, respectively. We take

$$\hat{U}_{\boldsymbol{R}} \equiv \hat{U}(\theta_{\boldsymbol{R}}) = \frac{1}{\sqrt{2}}\begin{bmatrix} e^{i\frac{2\pi}{3}\theta_{\boldsymbol{R}}} & e^{-i\frac{2\pi}{3}\theta_{\boldsymbol{R}}} \\ -e^{i\frac{2\pi}{3}\theta_{\boldsymbol{R}}} & e^{-i\frac{2\pi}{3}\theta_{\boldsymbol{R}}}\end{bmatrix}. \tag{D7}$$

This makes the Hartree-Fock trial Hamiltonian become

$$\begin{aligned}\hat{H}_0 = &\left(-\frac{t}{2}\right)\sum_{\tilde{\tau}}\sum_{\langle\boldsymbol{R},\boldsymbol{R}'\rangle}\hat{\tilde{h}}_{\boldsymbol{R},\tilde{\tau}}\hat{\tilde{h}}^\dagger_{\boldsymbol{R}',\tilde{\tau}}\\ &+\frac{i\sqrt{3}t}{2}\sum_{\tilde{\tau},\tilde{\tau}'}\sum_{\langle\boldsymbol{R},\boldsymbol{R}'\rangle}\epsilon_{\boldsymbol{R}\boldsymbol{R}'}\hat{\tilde{h}}_{\boldsymbol{R},\tilde{\tau}}(\hat{\boldsymbol{\sigma}}_{\tilde{\tau},\tilde{\tau}'}\cdot\boldsymbol{e}_x)\hat{\tilde{h}}^\dagger_{\boldsymbol{R}',\tilde{\tau}'}\\ &-h_Z\sum_{\tilde{\tau},\tilde{\tau}'}\sum_{\boldsymbol{R}}\hat{\tilde{h}}_{\boldsymbol{R},\tilde{\tau}}(\hat{\boldsymbol{\sigma}}_{\tilde{\tau},\tilde{\tau}'}\cdot\boldsymbol{e}_z)\hat{\tilde{h}}^\dagger_{\boldsymbol{R},\tilde{\tau}'},\end{aligned} \tag{D8}$$

where $\epsilon_{\boldsymbol{R}\boldsymbol{R}'}$ is the antisymmetric tensor defined in Appendix B. In momentum-space representation, we have

$$\begin{aligned}\hat{H}_0 = \sum_{\tau,\tau'}\sum_{\boldsymbol{k}}\hat{\tilde{h}}_{\boldsymbol{k},\tau}[&-t\gamma_{\boldsymbol{k}} - h_Z(\hat{\boldsymbol{\sigma}}_{\tau\tau'}\cdot\boldsymbol{e}_z)\\ &-\sqrt{3}th_{\boldsymbol{k}}(\hat{\boldsymbol{\sigma}}_{\tau\tau'}\cdot\boldsymbol{e}_x)]\hat{\tilde{h}}^\dagger_{\boldsymbol{k},\tau'},\end{aligned} \tag{D9}$$

with $h_{\boldsymbol{k}}$ defined in Eq. (21). The spectrum of $\hat{H}_0$ follows directly as $\epsilon_{\boldsymbol{k},\zeta} = -t\gamma_{\boldsymbol{k}} + \zeta\Upsilon_{\boldsymbol{k}}$ with the Hartree-Fock bands labeled by $\zeta = \pm 1$. The energy splitting is given by

$$\Upsilon_{\boldsymbol{k}} = \sqrt{h_Z^2 + 3t^2h_{\boldsymbol{k}}^2}. \tag{D10}$$

The eigenmodes $\hat{\tilde{h}}_{\boldsymbol{k},\zeta}$ are described by $\hat{\tilde{h}}^\dagger_{\boldsymbol{k},\tau} = \sum_\zeta W_{\tau\zeta}(\boldsymbol{k})\hat{\tilde{h}}^\dagger_{\boldsymbol{k},\zeta}$ with the following transformation coefficients:

$$W_{\tau\zeta}(\boldsymbol{k}) = (\zeta\,\mathrm{sgn}[h_{\boldsymbol{k}}])^{\frac{1-\tau}{2}}\sqrt{\frac{1}{2}\left[1-\tau\zeta\frac{h_Z}{\Upsilon_{\boldsymbol{k}}}\right]}. \tag{D11}$$

These relations simplify Eq. (D6) to

$$h_Z = \frac{U}{2N}\sum_{\boldsymbol{k}}\frac{h_Z}{\Upsilon_{\boldsymbol{k}}}, \tag{D12}$$

which allows for determination of h_Z. As $U \gg t$, we have $h_Z \simeq \frac{U}{2}$.

The dressed holon dispersion discussed in the main text should correspond to a particle-hole transformation to the $\zeta = -1$ band in the context of Hartree-Fock calculation, which gives

$$\epsilon_k^{(\mathrm{HF})} = t\gamma_k + \frac{U}{2}\sqrt{1 + 12\left(\frac{th_k}{U}\right)^2} \simeq \frac{U}{2} + \left(t - \frac{3J}{2}\right)\gamma_k + \frac{3J}{4}\tilde{\gamma}_k - \frac{3J}{4}\gamma_{2k} \tag{D13}$$

in the limit $U \gg t$. This dispersion is equivalent to Eq. (24) up to an overall constant, and we identify that $2t_1 = -t + 3J/2$, $2t_2 = -3J/4$, and $2t_3 = 3J/4$.

APPENDIX E: CURRENT OPERATOR AND OPTICAL CONDUCTIVITY FOR MOTT-MOIRÉ EXCITON

In this Appendix, we discuss the derivation of current operator (29) in Sec. III.

To start with, the low-energy physics for Bloch electrons near the valleys within monolayer TMDs is modeled by the massive Dirac fermion model [2]. Hence, we describe twisted TMD bilayer as a monolayer system experiencing the moiré potentials from the other layer, meaning that the low-energy physics of valley τ and layer l is given by

$$\hat{H}_{l,\tau} = \begin{bmatrix} E_l^g/2 & v_l^F(\tau\hat{p}_{l,x} - i\hat{p}_{l,y}) \\ v_l^F(\tau\hat{p}_{l,x} + i\hat{p}_{l,y}) & -E_l^g/2 \end{bmatrix} + \Delta_l(\boldsymbol{r}_l) + \hat{H}_{\mathrm{SO}}, \tag{E1}$$

where the basis states for the matrix are the orbitals of electrons in the conduction and valence bands, respectively. v_l^F, E_l^g, and $\Delta_l(\boldsymbol{r}_l)$ are the Fermi velocity, the band gap, and the moiré potential of layer l, respectively. $\hat{\boldsymbol{p}}_l$ denotes the momentum operator measured from the valleys and $\boldsymbol{r}_l$ is the position variable for each layer. Note that $\boldsymbol{r}_l$ is discretized by a_l, the lattice spacing of layer l, it is often treated as continuous since a_l is much smaller than the periodicity of the moiré potential a_M for small twist angles [20]. $\hat{H}_{\mathrm{SO}}$ denotes the spin-orbit coupling term that is responsible for spin-valley locking of low-energy degrees of freedom in TMD.

The moiré length scale a_M splits the Brillouin zone for the monolayers into small mBZs. Hence, it is sufficient to consider $\boldsymbol{p}_l$ within the first mBZ such that Eq. (E1) reduces to the decoupled moiré Hamiltonians for the valence and conduction bands, which are folded by the moiré potential into valence and conduction moiré bands, respectively. Focusing on $c1$ and $v1$ bands, which can be described by tight-binding/Hubbard models [24,35], we see that Eq. (E1) becomes Eq. (1).

To derive the expression (29), we replace the momentum operator with $\hat{\boldsymbol{p}}_l \to \hat{\boldsymbol{p}}_l + (e/c)\boldsymbol{A}$, where c is the speed of light and $\boldsymbol{A}$ is the vector potential, and take the functional derivative of the Hamiltonian (E1) with respective to $\boldsymbol{A}$. Next, we outline the derivation from Eq. (29) to the optical conductivity (30). We consider LSW to linearize Eq. (B1) for simplicity, and ignore all spin fluctuations in the current. In other words, we consider only the classical 120° spin-ordered state for the spin sector since this dominates in the light-matter coupling $\hat{H}_{\mathrm{opt}} \sim \hat{\boldsymbol{j}} \cdot \boldsymbol{A}$, as long as the strength of the vector potential $\boldsymbol{A}$ is small.

From Eq. (B1), within LSW treatment, the slave-fermion substitution (7) for the $v1$ hole creation operator follows as

$$\hat{h}^\dagger_{\boldsymbol{R},\tau} = \frac{1}{\sqrt{2}} e^{i\tau\frac{2\pi\theta_{\boldsymbol{R}}}{3}}(1 - \tau\hat{a}_{\boldsymbol{R}})\hat{\psi}^\dagger_{\boldsymbol{R}} \tag{E2}$$

with $\theta_{\boldsymbol{R}}$ for the three sublattices as defined in Appendix B. The current operator (29) then becomes

$$\hat{\boldsymbol{j}}^{(cv)} \simeq \frac{ev_F}{c}\sum_{\boldsymbol{k},\tau}\boldsymbol{e}_\tau \hat{c}^\dagger_{\boldsymbol{k},\tau}\hat{\psi}^\dagger_{-\boldsymbol{k}-\tau\boldsymbol{\kappa}} + \mathrm{H.c.}, \tag{E3}$$

in which we neglect the spin-fluctuation term $\hat{c}^\dagger\hat{\psi}^\dagger\hat{a}$, as mentioned previously, and we use the properties of the sublattice plane-wave factor $e^{i\tau\frac{2\pi\theta_{\boldsymbol{R}}}{3}} = e^{-i\tau\boldsymbol{\kappa}\cdot\boldsymbol{R}}$ with $\boldsymbol{\kappa} = -\frac{4\pi}{3}\boldsymbol{e}_x$ the momentum labeling κ in mBZ (in units of a_M^{-1}), assuming the origin $\boldsymbol{R} = 0$ takes $\theta_{\boldsymbol{R}} = 0$. We proceed to rewrite Eq. (E3) in terms of exciton operator (3):

$$\hat{\boldsymbol{j}}^{(cv)} \simeq \frac{\sqrt{N}ev_F}{c}\sum_{n,\tau}\boldsymbol{e}_\tau\Phi^{(n)}_{-\tau\boldsymbol{\kappa}}\hat{X}_{n,\tau}(-\tau\boldsymbol{\kappa}) + \mathrm{H.c.}, \tag{E4}$$

in which we use $\Phi^{(n)}_{\boldsymbol{Q}} = \frac{1}{\sqrt{N}}\sum_{\boldsymbol{p}}\phi^{(n)}_{\boldsymbol{Q}}(\boldsymbol{p})$. The optical matrix element [17] for the Mott-moiré exciton state $\hat{X}_{n,\tau}(\boldsymbol{Q})$, denoted as $\boldsymbol{J}_{n,\tau}(\boldsymbol{Q})$, is then

$$\boldsymbol{J}_{n,\tau}(\boldsymbol{Q}) \equiv \frac{1}{\sqrt{\mathcal{A}}}\langle\mathrm{GS}|\hat{\boldsymbol{j}}^{(cv)}\hat{X}^\dagger_{n,\tau}(\boldsymbol{Q})|\mathrm{GS}\rangle = \sqrt{\frac{N}{\mathcal{A}}}\frac{ev_F}{c}\delta_{\boldsymbol{Q},-\tau\boldsymbol{\kappa}}\boldsymbol{e}_\tau\Phi^{(n)}_{-\tau\boldsymbol{\kappa}}, \tag{E5}$$

where $\mathcal{A}$ denotes the system area such that $\mathcal{A}/N$ gives the area of unit moiré cell, and $|GS\rangle$ is the exciton ground state. The optical conductivity from linear response theory [87] follows as $\sigma_{ij}(\omega) = \sigma(\omega)\delta_{ij}$, where

$$\sigma(\omega) \simeq \frac{i}{\omega}\sum_{n,\tau,\boldsymbol{Q}}\frac{|\boldsymbol{J}_{n,\tau}(\boldsymbol{Q})|^2}{\omega - E^X_{n,\boldsymbol{Q}} + i\delta_+}, \tag{E6}$$

where we neglect the branch with $\omega + E^X_{n,\boldsymbol{Q}} + i\delta_+$ since we are interested near resonance, i.e., $\omega \simeq E^X_{n,\boldsymbol{Q}}$. Putting Eq. (E5) into (E6), we arrive at Eq. (30).

APPENDIX F: OPTICAL CONDUCTIVITY FOR MOIRÉ EXCITON

For moiré excitons (i.e., the absence of intraband correlation), the interband current operator at zero momentum is

$$\hat{\boldsymbol{j}}^{(cv)} = \frac{\sqrt{2}ev_F}{c}\sum_{\boldsymbol{k},\tau}\hat{e}_\tau\hat{c}^\dagger_{\boldsymbol{k},\tau}\hat{h}^\dagger_{\boldsymbol{k},\tau} + \mathrm{H.c.} \tag{F1}$$

and similar to Eq. (3) for Mott-moiré exciton, we define the moire exciton operator as

$$\hat{X}_{n,\tau}(\boldsymbol{Q}) = \sum_{\boldsymbol{p}}\phi^{(n)}_{\boldsymbol{Q}}(\boldsymbol{p})\hat{h}_{-\frac{\boldsymbol{Q}}{2}+\boldsymbol{p},\tau}\hat{c}_{\frac{\boldsymbol{Q}}{2}+\boldsymbol{p},\tau}, \tag{F2}$$

where ϕ in this Appendix denotes the moiré exciton wave function. The current from moiré exciton follows as

$$\boldsymbol{j}^{(cv)} = \frac{\sqrt{2N}ev_F}{c}\sum_{n,\tau}\hat{e}_\tau\Phi^{(n)}_0\hat{X}^\dagger_{n,\tau} + \mathrm{H.c.}, \tag{F3}$$

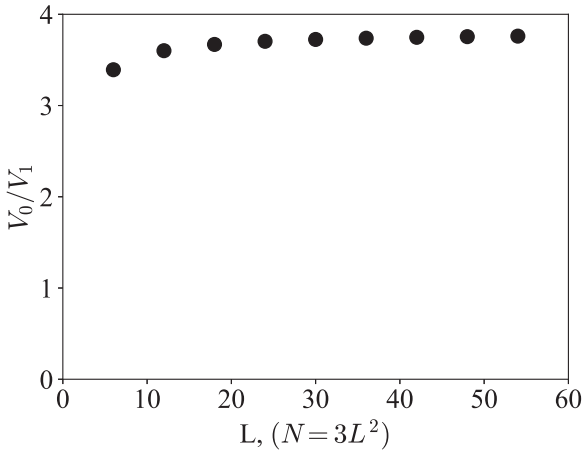

FIG. 21. Ratio between V_0 and V_1 from Eq. (26) for different system sizes $N = 3L^2$. As $\boldsymbol{q}$ is summed over mBZ, V_0/V_1 asymptotically approaches a specific value.

where $\hat{X}^\dagger_{n,\tau} \equiv \hat{X}^\dagger_{n,\tau}(0)$ and $\Phi_0^{(n)} = \frac{1}{\sqrt{N}} \sum_{\boldsymbol{p}} \phi_0^{(n)}(p)$. Similar to the calculation presented in Appendix E, we obtain the optical conductivity for moiré exciton as $\sigma_{ij}(\omega) = \sigma(\omega)\delta_{ij}$ with

$$\sigma(\omega) \sim \frac{i}{\omega} \sum_{n,\tau} \frac{\left|\Phi_0^{(n)}\right|^2}{\omega - E^X_{n,0} + i0_+}, \tag{F4}$$

where in this Appendix $E^X_{n,0}$ denotes the energy of moiré exciton at zero total momentum.

APPENDIX G: PERTURBATION THEORY ON WANNIER EQUATION FOR EXCITONS IN TMD HETEROBILAYER

In this Appendix, we discuss the perturbation theory on Eq. (27) in detail. First, we point out that the total momentum $\boldsymbol{Q}$ is a good quantum number of the Hamiltonian operator in Eq. (27), meaning that the energy eigenstates are also eigenstates of $\boldsymbol{Q}$. Thus, these energy eigenstates can be labeled as $|n, \boldsymbol{Q}\rangle$, with n labeling the internal states. We suppress the valley degeneracy throughout the discussion in this Appendix.

We consider the strong interacting limit for perturbation, i.e. $\langle \varepsilon_{\boldsymbol{Q}}(\boldsymbol{p})\rangle_{n,\boldsymbol{Q}} \ll \langle V(q)\rangle_{n,\boldsymbol{Q}}$. We also emphasize that such a limit is of interest in our work as the exciton dispersion is flat compared to the Coulomb binding for both Mott-moiré and moiré excitons, as indicated by Fig. 3. The unperturbed term in the Hamiltonian for Eq. (27) is then the Coulomb attraction term $V(q)$, which gives unperturbed states as eigenstates of the relative distance operator $\hat{r}$ according to the position-space representation of $V(q)$. Hence, we have $|n, \boldsymbol{Q}\rangle \simeq |j, \boldsymbol{Q}\rangle$ in the strong interacting limit, where j are non-negative integers that label $|\boldsymbol{r}|$ in nondescending order.

The unperturbed ground state is the state with $|\boldsymbol{r}| = 0$, denoted as $|0, \boldsymbol{Q}\rangle$. We denote the unperturbed energy for this state as $-V_0$, which we estimate to be $\mathcal{A}^{-1} \sum_{\boldsymbol{q}} V(q) \simeq 3.7V_1$ with $\boldsymbol{q}$ summed over mBZ and $N = 3\times 24^2$ (see Fig. 21), since we are assuming the electrons and holes are tightly bound to moiré sites. We expect this estimation to capture the correct qualitative properties with this perturbation scheme since we have $V_0 \gg t$ using the above expression. In reality, we expect a smaller V_0 due to the finite width of Wannier functions of the quasiparticles, but we expect V_0 to be of order U in this case and hence $V_0 \gg t$ is still valid.

The first-order correction on ground-state energy $\delta E^{X,(1)}_{0,\boldsymbol{Q}} = \langle \varepsilon_{\boldsymbol{Q}}(\boldsymbol{p})\rangle_{0,\boldsymbol{Q}}$ is zero. This comes from the fact that the momentum-space wave function of the unperturbed ground state $\langle p, \boldsymbol{Q}|0, \boldsymbol{Q}\rangle = N^{-1/2}$ is just a constant, and that $\varepsilon_{\boldsymbol{Q}}(\boldsymbol{p})$ is composed of sinusoidal functions, for both Mott-moiré and moiré excitons. Hence, the leading-order correction to the ground-state energy is at least second order.

Calculations of the second-order correction $\delta E^{X,(2)}_{0,\boldsymbol{Q}}$ require the information of unperturbed excited states. The first few unperturbed excited states are labeled as $|1, \boldsymbol{Q}\rangle$, $|2, \boldsymbol{Q}\rangle$, and $|3, \boldsymbol{Q}\rangle$, which has well-defined relative distance $|\boldsymbol{r}| = 1, \sqrt{3}$, and 2 (in units of a_M), respectively. We denote the corresponding energies as $-V_{1,2,3}$, of which magnitude are much smaller than V_0. Note that we suppress the label for the sixfold degeneracy for each $|j > 0, \boldsymbol{Q}\rangle$ for simplicity. We then proceed for the second-order correction $\delta E^{X,(2)}_{0,\boldsymbol{Q}}$, which involves matrix elements $\langle j, \boldsymbol{Q}|\varepsilon_{\boldsymbol{Q}}(\boldsymbol{p})|0, \boldsymbol{Q}\rangle$ for $j > 0$.

We start with the perturbation for moiré excitons. For moiré excitons, only $j = 1$ contributes since the position-space representation of $\varepsilon_{\boldsymbol{Q}}(\boldsymbol{p})$ contains only nearest-neighboring hopping terms. We then obtain

$$\langle 1, \boldsymbol{Q}|\varepsilon_{\boldsymbol{Q}}(\boldsymbol{p})|0, \boldsymbol{Q}\rangle = (-2t)\cos\left(\pm\frac{\boldsymbol{Q}}{2}\cdot\boldsymbol{e}_i\right), \tag{G1}$$

where $\boldsymbol{e}_i$ are nearest-neighboring vectors defined below Eq. (18). The second-order correction for moiré excitons follows as

$$\delta E^{X,(2)}_{0,\boldsymbol{Q}} = -\frac{4t^2}{V_0 - V_1}\gamma_{\boldsymbol{Q}} - \frac{12t^2}{V_0 - V_1}. \tag{G2}$$

The situation is slightly more complicated for Mott-moiré excitons, in which terms with $j = 1, 2, 3$ would contribute to $\delta E^{X,(2)}_{0,\boldsymbol{Q}}$. Nevertheless, only the $j = 1$ term contributes to the exciton bandwidth W_X. Direct evaluation gives

$$\langle 1, \boldsymbol{Q}|\varepsilon_{\boldsymbol{Q}}(\boldsymbol{p})|0, \boldsymbol{Q}\rangle = (-t - t_1)\cos\left(\pm\frac{\boldsymbol{Q}}{2}\cdot\boldsymbol{e}_i\right) + i(t - t_1)\sin\left(\pm\frac{\boldsymbol{Q}}{2}\cdot\boldsymbol{e}_i\right), \tag{G3}$$

$$\langle 2, \boldsymbol{Q}|\varepsilon_{\boldsymbol{Q}}(\boldsymbol{p})|0, \boldsymbol{Q}\rangle = (-2t_2)e^{i\frac{\boldsymbol{Q}}{2}\cdot\boldsymbol{r}_2}, \tag{G4}$$

$$\langle 3, \boldsymbol{Q}|\varepsilon_{\boldsymbol{Q}}(\boldsymbol{p})|0, \boldsymbol{Q}\rangle = (-t_3)e^{i\frac{\boldsymbol{Q}}{2}\cdot\boldsymbol{r}_3}, \tag{G5}$$

where $\boldsymbol{r}_{2,3}$ denotes the relative separation for states with $j = 2, 3$, respectively. Consequently, the second-order correction for Mott-moiré excitons is

$$\delta E^{X,(2)}_{0,\boldsymbol{Q}} = -\frac{6\left(t^2 + t_1^2\right)}{V_0 - V_1} - \frac{6t_2^2}{V_0 - V_2} - \frac{6t_3^2}{V_0 - V_3} - \frac{4tt_1}{V_0 - V_1}\gamma_{\boldsymbol{Q}}. \tag{G6}$$

Comparing the results for moiré exciton and Mott-moiré exciton, the ratio between their bandwidths is

$$\frac{W_X^{Mm}}{W_X^m} = \left|\frac{t_1}{t}\right| \ll 1, \tag{G7}$$

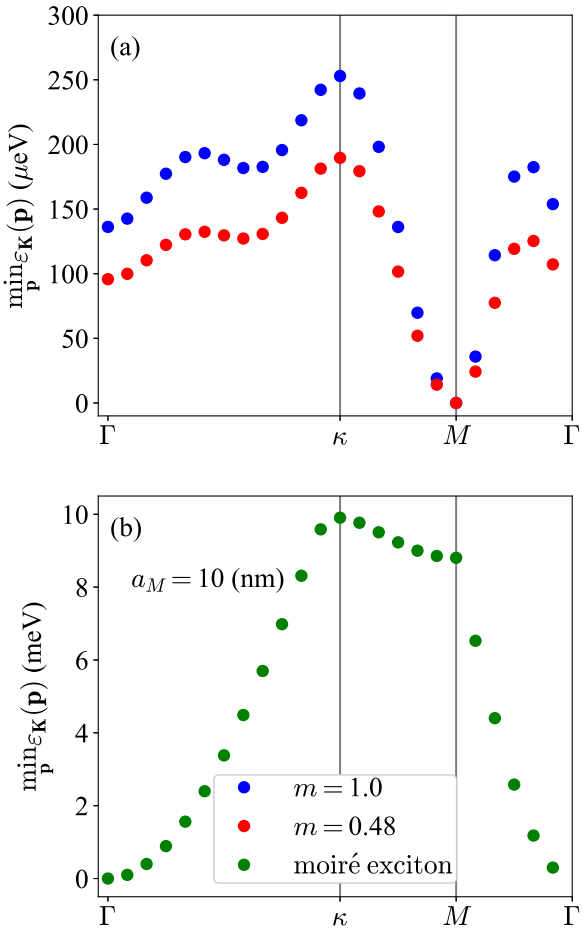

FIG. 22. Center-of-mass motion for the lowest internal states for the free two-particle system, i.e., not affected by mutual Coulomb attraction, of a lattice of size 3×24×24 in the case with (top) and without (bottom) Mott physics. The moiré period is set as $a_M =$ 10 (nm). In the case without Mott physics, the hole motion is described by $\hat{H}_v \to (-2t)\sum_k \gamma_k \hat{h}^\dagger_{k,\tau}\hat{h}_{k,\tau}$ in Eq. (2).

where W_X^{Mm} and W_X^m denote the bandwidths of lowest Mott-moiré exciton and moiré exciton, respectively. Comparison between numerical and perturbation results is shown in Fig. 12.

Next, we continue to use this perturbative analysis to investigate the exciton binding energy. We start from the qualitative observation that correction to exciton energy $E^X_{0,\boldsymbol{Q}}$ is at most of order t^2/V_0 for both Mott-moiré and moiré excitons. Hence, up to linear order in t, we can approximate $E^X_{0,\boldsymbol{Q}} \simeq -V_0 - \mu$, where μ denotes the chemical potential that is set differently for the two types of excitons. Recall that we define the exciton binding energy as the energy reduction from the lowest-branch unbound two-particle kinetic energy to the exciton energy, i.e., $E^B_{0,\boldsymbol{Q}} \equiv \min_{\boldsymbol{p}} \varepsilon_{\boldsymbol{Q}}(\boldsymbol{p}) - E^X_{0,\boldsymbol{Q}}$ with $\varepsilon_{\boldsymbol{Q}}(\boldsymbol{p})$ as the unbound two-particle kinetic energy defined in Eq. (28). This definition reflects that the Coulomb binding conserves the total momentum $\boldsymbol{Q}$. An example of $\min_{\boldsymbol{p}} \varepsilon_{\boldsymbol{Q}}(\boldsymbol{p})$ is plotted in Fig. 22, suggesting that the width of $\min_{\boldsymbol{p}} \varepsilon_{\boldsymbol{Q}}(\boldsymbol{p})$ in $\boldsymbol{Q}$ is of order J for Mott-moiré exciton and of order t for moiré exciton. From direct calculations, we find that to the linear order in t, $\min_{\boldsymbol{p}} \varepsilon_{\boldsymbol{Q}}(\boldsymbol{p})$ is $-6t - \mu$ for Mott-moiré exciton and $-2t\gamma_{\boldsymbol{Q}} - 6t - \mu$ for moiré exciton. Hence, to the linear order in t, the Mott-moiré exciton binding energy is $E^B_{0,\boldsymbol{Q}} \simeq V_0 - 6t$, while for moiré exciton it is $E^B_{0,\boldsymbol{Q}} \simeq V_0 - 6t - 2t\gamma_{\boldsymbol{Q}}$, which is $V_0 - 3t$ at $\boldsymbol{Q} = \boldsymbol{\kappa}$. This explains the slightly larger binding for moiré exciton, as illustrated in Fig. 3(a). We end by pointing out that the non-negligible dependence of binding energy on total momentum $\boldsymbol{Q}$ for moiré exciton is very different from the case for hydrogenic exciton [73]. This is because the center-of-mass degrees of freedom can be separated from the relative motion for hydrogenic exciton, while these degrees of freedoms are not separable for excitons derived from the moiré superlattice [88].

APPENDIX H: EXCITON EXCHANGE INTERACTION

In this Appendix, we discuss the role of exchange interaction on the Mott-moiré exciton spectrum following standard procedures [64]. Such vertex emerges microscopically from the Coulomb potential between electrons:

$$\hat{V}_C = \frac{1}{2}\int_{\boldsymbol{r}_1,\boldsymbol{r}_2} \hat{\psi}^\dagger(\boldsymbol{r}_1)\hat{\psi}(\boldsymbol{r}_1)V(r_{12})\hat{\psi}^\dagger(\boldsymbol{r}_2)\hat{\psi}(\boldsymbol{r}_2), \tag{H1}$$

where $r_{12} = |\boldsymbol{r}_1 - \boldsymbol{r}_2|$, $\int_{\boldsymbol{r}_1,\boldsymbol{r}_2} = \int d^2\boldsymbol{r}_1 d^2\boldsymbol{r}_2$, and $\boldsymbol{r}_{1,2}$ denote continuous position variables. $V(r_{12})$ characterizes the electrostatic interaction, which we take as the Fourier transform of Eq. (26). We consider Eq. (H1) on top of the superlattice. According to Bloch theorem, the electron field operator $\hat{\psi}(\boldsymbol{r})$ in the moiré band basis is

$$\hat{\psi}(\boldsymbol{r}) = \sum_{\boldsymbol{P},\lambda,\tau} \psi_{\lambda,\boldsymbol{P},\tau}(\boldsymbol{r})\hat{f}_{\lambda,\boldsymbol{P},\tau}, \tag{H2}$$

where λ denotes the moiré band index and $\boldsymbol{P}$ is the superlattice momentum. $\hat{f}_{\lambda,\boldsymbol{P},\tau}$ represents the electron annihilation operator for a specific moiré-Bloch state and $\psi_{\lambda,\boldsymbol{P},\tau}(\boldsymbol{r})$ stands for the associated wave function. The exchange interaction between charges in $\lambda \neq \lambda'$ bands, $\hat{V}^{\lambda,\lambda'}_{\text{exc}} + \hat{V}^{\lambda',\lambda}_{\text{exc}}$, emerges as one of the terms appearing after plugging Eq. (H2) into (H1), where

$$\hat{V}^{\lambda,\lambda'}_{\text{exc}} = \sum_{\tau\tau'}\sum_{\boldsymbol{P}\boldsymbol{P}'\boldsymbol{Q}} J^{\tau,\tau';\lambda,\lambda'}_{\boldsymbol{P},\boldsymbol{P}';\boldsymbol{Q}} \hat{\Pi}^{\lambda,\lambda'\dagger}_{\boldsymbol{P},\tau;\boldsymbol{Q}}\hat{\Pi}^{\lambda,\lambda'}_{\boldsymbol{P}',\tau';\boldsymbol{Q}}, \tag{H3}$$

where the electron-hole-pair operator (with total and relative momentum $\boldsymbol{Q}$ and $\boldsymbol{P}$) is

$$\hat{\Pi}^{\lambda,\lambda'\dagger}_{\boldsymbol{P},\tau;\boldsymbol{Q}} = \hat{f}^\dagger_{\lambda,\boldsymbol{P}+\frac{\boldsymbol{Q}}{2},\tau}\hat{f}_{\lambda',\boldsymbol{P}-\frac{\boldsymbol{Q}}{2},\tau}, \tag{H4}$$

and the exchange matrix element has the following expression:

$$J^{\tau,\tau';\lambda,\lambda'}_{\boldsymbol{P},\boldsymbol{P}';\boldsymbol{Q}} = \frac{1}{2\mathcal{A}}\sum_{\boldsymbol{G}} V(\boldsymbol{Q}+\boldsymbol{G})\Pi^{\lambda,\lambda'*}_{\boldsymbol{P},\tau;\boldsymbol{Q}}(\boldsymbol{G})\Pi^{\lambda,\lambda'}_{\boldsymbol{P}',\tau';\boldsymbol{Q}}(\boldsymbol{G}), \tag{H5}$$

where $\boldsymbol{G}$ denotes reciprocal superlattice vectors and $\mathcal{A}$ is the system area. $V(\boldsymbol{Q})$ follows Eq. (26) and the pair function is

$$\Pi^{\lambda,\lambda'}_{\boldsymbol{P},\tau;\boldsymbol{Q}}(\boldsymbol{G}) = \int d^2\boldsymbol{r}\, e^{-i\boldsymbol{G}\cdot\boldsymbol{r}} u_{\lambda,\boldsymbol{P}+\frac{\boldsymbol{Q}}{2},\tau}(\boldsymbol{r})u^*_{\lambda',\boldsymbol{P}-\frac{\boldsymbol{Q}}{2},\tau}(\boldsymbol{r}), \tag{H6}$$

with $u_{\lambda,\boldsymbol{P},\tau}(\boldsymbol{r}) = e^{-i\boldsymbol{P}\cdot\boldsymbol{r}}\psi_{\lambda,\boldsymbol{P},\tau}(\boldsymbol{r})$ being moiré-Bloch functions. We further separate the $\boldsymbol{G}$ summation in Eq. (H5) into two sectors: the *long-ranged* (LR) and *short-ranged* (SR) parts with $\boldsymbol{G} = 0$ and $\boldsymbol{G} \neq 0$, respectively. We assume the short-ranged

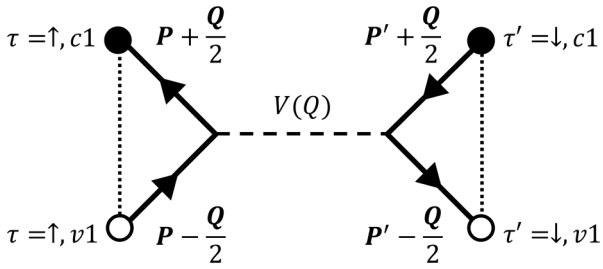

FIG. 23. Feynman diagram for exchange scattering between Mott-moiré (and moiré) excitons at different valleys. Black and white circles connected to solid lines indicate electrons and holes, respectively. Dotted line connects charges that eventually bind into an exciton. Dashed line represents Coulomb interaction $V(Q)$. The vertex originates Eq. (H3) with $\lambda = c1$, $\lambda' = v1$, $\tau = \uparrow$, and $\tau' = \downarrow$, contributing to Eq. (H10) in the exciton basis.

sector is dominant by the terms with $Q \ll G$ and accordingly take $\boldsymbol{Q} \to 0$ as an approximation. Hence, we have

$$J^{\tau,\tau';\lambda,\lambda'}_{\boldsymbol{P},\boldsymbol{P}';\boldsymbol{Q}} \simeq J^{\tau,\tau';\lambda,\lambda'}_{LR;\boldsymbol{P},\boldsymbol{P}'}(\boldsymbol{Q}) + J^{\tau,\tau';\lambda,\lambda'}_{SR;\boldsymbol{P},\boldsymbol{P}'}, \tag{H7}$$

$$J^{\tau,\tau';\lambda,\lambda'}_{LR;\boldsymbol{P},\boldsymbol{P}'}(\boldsymbol{Q}) = \frac{1}{2\mathcal{A}} V(\boldsymbol{Q}) \Pi^{\lambda,\lambda'*}_{\boldsymbol{P},\tau;\boldsymbol{Q}}(0) \Pi^{\lambda,\lambda'}_{\boldsymbol{P}',\tau';\boldsymbol{Q}}(0), \tag{H8}$$

$$J^{\tau,\tau';\lambda,\lambda'}_{SR;\boldsymbol{P},\boldsymbol{P}'} = \frac{1}{2\mathcal{A}} \sum_{\boldsymbol{G}\neq 0} V(\boldsymbol{G}) \Pi^{\lambda,\lambda'*}_{\boldsymbol{P},\tau;0}(\boldsymbol{G}) \Pi^{\lambda,\lambda'}_{\boldsymbol{P}',\tau';0}(\boldsymbol{G}), \tag{H9}$$

where Eq. (H8) captures the long-range exchange processes while Eq. (H9) describes similar but short-range scattering.

We first discuss the role for exchange on moiré excitons from $c1$ and $v1$ bands, modeled by the full Hamiltonian $\hat{H} = \hat{H}_X + \hat{V}^{c1,v1}_{\text{exc}}$ (we drop $\hat{V}^{v1,c1}_{\text{exc}}$ for its suppression with dilute $c1$ electrons). $\hat{H}_X$ involves the single-particle energies of electrons and holes and density-density attraction between them, which eventually gives an exciton Hamiltonian diagonal in $\boldsymbol{Q}$ and τ [similar to the expression in Eq. (4)]. We also assume such sector to predominantly determine the profile of exciton wave functions such that the associated operators still follow Eq. (F2). Upon a basis transformation from electron-hole pair to exciton (we relate the fermion operators by $\hat{f}_{c1,\boldsymbol{P},\tau} = \hat{c}_{\boldsymbol{P},\tau}$ and $\hat{f}_{v1,\boldsymbol{P},\tau} = \hat{h}^\dagger_{-\boldsymbol{P},\tau}$), the exchange interaction is

$$\hat{V}^{c1,v1}_{\text{exc}} = \sum_{\tau\tau'} \sum_{n,\boldsymbol{Q}} J^{\tau,\tau'}_{n,\boldsymbol{Q}} \hat{X}^\dagger_{n,\tau}(\boldsymbol{Q}) \hat{X}_{n,\tau'}(\boldsymbol{Q}), \tag{H10}$$

where we drop the off-diagonal terms in n since their energy corrections are suppressed by the splittings between these levels (which are significant for the first few states due to the large binding). Notably, it provides not only intravalley but also intervalley exciton scattering in general (see Fig. 23). The exchange couplings for moiré excitons are

$$J^{\tau,\tau'}_{n,\boldsymbol{Q}} = \sum_{\boldsymbol{P}\boldsymbol{P}'} J^{\tau,\tau';c1,v1}_{\boldsymbol{P},\boldsymbol{P}';\boldsymbol{Q}} \phi^{(n)}_{\boldsymbol{Q}}(\boldsymbol{P}) \phi^{(n)*}_{\boldsymbol{Q}}(\boldsymbol{P}'). \tag{H11}$$

We focus on the s-wave states, which are bright at $\boldsymbol{Q} = 0$. Importing Eq. (H7) into $J^{\tau,\tau'}_{n,\boldsymbol{Q}}$, its expression separates into LR and SR pieces. Upon a $\boldsymbol{k}\cdot\boldsymbol{p}$ approximation on the moiré-Bloch functions, the LR sector becomes $\sim Q^2 V(Q)$, similar to the results for excitons in monolayer TMDs [5,64]. Notably, the gap between $c1$ and $v1$ bands participates in the denominator of the proportionality constant [64].

The SR sector of Eq. (H11) for s-wave states is completely suppressed by the $C3$ rotational symmetry, which manifests for excitons not only in monolayer TMDs [64] but also in moiré ones [20,22] centered around supersites. To discuss rotational symmetry of Bloch functions, we adopt the envelope function approximation [73]. In this context, Wannier functions of charges can be viewed as product of atomic orbital (labeled by $\eta \in \{c, v\}$) and the ladders from moiré potential (labeled by $\Lambda = \{1, 2, 3, \dots\}$), governing spatial variation at the scales of monolayer lattice and a_M, respectively. Accordingly, $\lambda = \eta\Lambda$ (e.g., $\lambda = c1$ is equivalent to $\eta = c$ with $\Lambda = 1$). Under $C3$ rotation (denoted with $\hat{C}_3$), moiré-Bloch functions transform as

$$u_{\lambda,\hat{C}_3\boldsymbol{P},\tau}(\hat{C}_3\boldsymbol{r}) = e^{i\frac{2\pi}{3}[\tau l_\eta + l_\Lambda]} u_{\lambda,\boldsymbol{P},\tau}(\hat{C}_3\boldsymbol{r}), \tag{H12}$$

where l_Λ denotes the angular momentum from the moiré orbital, and $\tau l_c = \tau(l_v + 1)$ and τl_c are those from atomic orbitals [20]. Note that these angular momenta are τ dependent, which is the origin of valley selectivity. The phase factors in Eq. (H12) are essential in determining whether the SR sector of Eq. (H10) is zero. In particular, for bright moiré excitons giving $\phi^{(n)}_0(\hat{C}_3\boldsymbol{P}) = \phi^{(n)}_0(\boldsymbol{P})$, such matrix element is trivial unless $(\tau' - \tau)(l_\eta - l_{\eta'}) = 0$. Accordingly, intervalley SR exciton exchange (within charges at $c1$ and $v1$) is absent. Combining with the results for LR exchange, we find absent exchange coupling for bright moiré excitons at different valleys.

Derivation for exchange on Mott-moiré excitons follow similar procedures. The only difference is that these bound states are electron-holon pairs, which exhibits a $\boldsymbol{\kappa}$ total momentum shift from electron-hole pairs due to the 120° spin order [see Eq. (E2) and discussion below]. Accordingly, their LR exchange matrix elements become $\sim(\Delta\boldsymbol{Q})^2 V(\Delta\boldsymbol{Q})$, where $\Delta\boldsymbol{Q}$ is the total momentum counted from the mBZ corners. In addition, since electron-holon pairs at $\boldsymbol{Q} = \boldsymbol{\kappa}$ and electron-hole pairs at $\boldsymbol{Q} = 0$ are equivalent, the absence of exchange coupling between bright Mott-moiré excitons at different valleys also applies.

We end this Appendix by summarizing the results and relevant experimental implications. For both Mott-moiré and moiré excitons, the momentum dependence of energy correction from exchange coupling (which predominantly comes from the LR sector) would be more suppressed by a larger band gap. For interlayer excitons, such energy scale is controllable with out-of-plane electric field [97]. This provides a way to reduce the effect of the LR exchange interaction on the exciton dispersion such that dropping it in Eq. (1) is legitimate. Accordingly, implications from the bandwidth of interlayer moiré excitons to the diffusion measurements [39–41] can be rendered unaffected. Another important remark is the absence of exchange coupling on the bright excitons, meaning that it does not affect optical measurements on these bound states. From these considerations, it is sufficient to neglect exchange interaction in our theoretical study for Mott-moiré excitons.

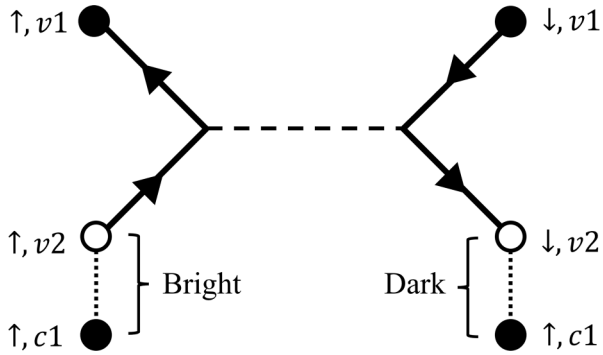

FIG. 24. Feynman diagram for exchange scattering between bright and dark spectator excitons [see second term of Eq. (I5)]. Notations follow Fig. 23.

APPENDIX I: SPECTATOR EXCITON

We formulate the spectator excitons and discuss the consequence of spin correlation on them in this Appendix. These bound states contain a conduction electron and a hole on generic valence moiré band except the half-filled $v1$, which demonstrates spin physics. For simplicity, we assume the electron is on $c1$ and denote the band index of the hole as $v2$. We focus on the lowest internal states of these composite particles. Focusing on these mini-bands according to the discussion in Sec. II, we take the following Hamiltonian as our minimum model:

$$\begin{aligned}\hat{H} = &\sum_{\tau}\sum_{\langle \boldsymbol{R},\boldsymbol{R}'\rangle}[-t\hat{c}^{\dagger}_{\boldsymbol{R},\tau}\hat{c}_{\boldsymbol{R}',\tau} - t'\hat{v}^{\dagger}_{\boldsymbol{R},\tau}\hat{v}_{\boldsymbol{R}',\tau}]\\ &-\sum_{\tau\tau'}\sum_{\boldsymbol{R}\boldsymbol{R}'}\tilde{V}_{|\boldsymbol{R}-\boldsymbol{R}'|}\hat{c}^{\dagger}_{\boldsymbol{R},\tau}\hat{v}^{\dagger}_{\boldsymbol{R}',\tau'}\hat{v}_{\boldsymbol{R}',\tau'}\hat{c}_{\boldsymbol{R},\tau}\\ &+\hat{H}_J + \hat{V}^{v1,v2}_{\rm exc} + \hat{V}^{v2,v1}_{\rm exc},\end{aligned} \tag{I1}$$

where $\hat{v}_{\boldsymbol{R},\tau} = \hat{f}^{\dagger}_{v2,\boldsymbol{R},\tau}$ is the $v2$-hole annihilation operator and t' denotes its hopping. We assume its orbital to center around the same superlattice sites as the $c1$ electrons and $v1$ holes for simplicity. $\tilde{V}_{|\boldsymbol{R}-\boldsymbol{R}'|} = V^{c1,v2}_{|\boldsymbol{R}-\boldsymbol{R}'|}$ captures the density-density interaction that binds the spectator exciton. We suppress the direct Coulomb interactions involving $v1$ band since they only contributes to chemical potential shifts. $\hat{H}_J$ is the Heisenberg Hamiltonian for $v1$ spins, following Eq. (6). Finally, we include exchange interactions (H3) to convey spin physics in $v1$ to charges in $v2$ (and hence the spectator excitons, see Fig. 24). Note that we anticipate similar processes between $c1$ and the valence moiré bands less dominant than $\hat{V}^{v1,v2}_{\rm exc} + \hat{V}^{v2,v1}_{\rm exc}$ and hence drop these contributions. Such terms feel suppression from the large band gap of order eV [1] (see discussion in Appendix H), while the gap between $v1$ and $v2$ bands is comparable to 10 meV [24].

We further simplify Eq. (I1) to describe spectator excitons. First, in the dilute exciton limit, we anticipate the bound states not to significantly affect spin configuration in $v1$. This suggests spin correlation therein follows predominantly $\hat{H}_J$. Accordingly, we simplify Eq. (I1) by averaging over the $v1$ spin states (denoted with $\langle \dots \rangle_{v1}$):

$$\begin{aligned}\hat{H} = &\sum_{\tau}\sum_{\langle \boldsymbol{R},\boldsymbol{R}'\rangle}[-t\hat{c}^{\dagger}_{\boldsymbol{R},\tau}\hat{c}_{\boldsymbol{R}',\tau} - t'\hat{v}^{\dagger}_{\boldsymbol{R},\tau}\hat{v}_{\boldsymbol{R}',\tau}]\\ &-\sum_{\tau\tau'}\sum_{\boldsymbol{R}\boldsymbol{R}'}\tilde{V}_{|\boldsymbol{R}-\boldsymbol{R}'|}\hat{c}^{\dagger}_{\boldsymbol{R},\tau}\hat{v}^{\dagger}_{\boldsymbol{R}',\tau'}\hat{v}_{\boldsymbol{R}',\tau'}\hat{c}_{\boldsymbol{R},\tau}\\ &+\left\langle \hat{V}^{v1,v2}_{\rm exc} + \hat{V}^{v2,v1}_{\rm exc}\right\rangle_{v1},\end{aligned} \tag{I2}$$

where we suppress $\hat{H}_J$ as it does not involve the degrees of freedom in $c1$ and $v2$. Second, the density-density interaction (assumed to be more significant than tunneling as for Mott-moiré excitons) should separate the bound-state levels. We focus on the lowest manifold, in which bound charges roughly live on the same supersite. Accordingly, the bound states are

$$\hat{x}^{\dagger}_{\boldsymbol{R},\tau} = \hat{c}^{\dagger}_{\boldsymbol{R},\tau}\hat{v}^{\dagger}_{\boldsymbol{R},\tau}, \tag{I3}$$

$$\hat{y}^{\dagger}_{\boldsymbol{R},\tau} = \hat{c}^{\dagger}_{\boldsymbol{R},\tau}\hat{v}^{\dagger}_{\boldsymbol{R},-\tau}. \tag{I4}$$

If the exchange interactions are absent, these states are degenerate, and $\hat{x}_{\boldsymbol{R},\tau}$ is optically bright while $\hat{y}_{\boldsymbol{R},\tau}$ is dark according to valley selectivity for excitons in TMDs [20]. The effective Hamiltonian for these degrees of freedom from Eq. (I2) becomes

$$\hat{H} = \hat{H}_{xy} + \sum_{\boldsymbol{R},\tau}\begin{bmatrix}\hat{x}_{\boldsymbol{R},\tau}\\ \hat{y}_{\boldsymbol{R},\tau}\end{bmatrix}^{\dagger}\begin{bmatrix}j^{\tau,\tau}_{\boldsymbol{R}} & j^{\tau,-\tau}_{\boldsymbol{R}}\\ j^{-\tau,\tau}_{\boldsymbol{R}} & j^{-\tau,-\tau}_{\boldsymbol{R}}\end{bmatrix}\begin{bmatrix}\hat{x}_{\boldsymbol{R},\tau}\\ \hat{y}_{\boldsymbol{R},\tau}\end{bmatrix}, \tag{I5}$$

where $\hat{H}_{xy}$ denotes the lowest spectator exciton dispersion from the first two lines of Eq. (I2). Notably, the second term in Eq. (I5) only couples the degrees of freedoms at the same $\boldsymbol{R}$ and τ. This is because exchange interaction between $v1$ and $v2$ preserves all $c1$-electron labels. With $\langle \hat{\boldsymbol{n}}_{\boldsymbol{R}+\boldsymbol{L},\tau}\rangle_{v1} = \frac{1}{2}$, the diagonal exchange matrix elements $j^{\tau,\tau}_{\boldsymbol{R}}$ contribute to a chemical potential shift. In contrast, the off-diagonal ones are

$$j^{\tau,-\tau}_{\boldsymbol{R}} = -2\tau\boldsymbol{e}_{-\tau}\cdot\sum_{\boldsymbol{L}} J_{\boldsymbol{L},\tau}\langle\hat{\boldsymbol{S}}_{\boldsymbol{R}+\boldsymbol{L}}\rangle_{v1}, \tag{I6}$$

recalling $\boldsymbol{e}_{-\tau} = -\tau(\boldsymbol{e}_x + i\tau\boldsymbol{e}_y)$ and $\hat{\boldsymbol{S}}_{\boldsymbol{R}+\boldsymbol{L}}$ is the $v1$-spin vector [see Eq. (6)]. The position-space coefficients follow:

$$J_{\boldsymbol{L},\tau} = \frac{1}{N^2}\sum_{\boldsymbol{P}\boldsymbol{P}'\boldsymbol{Q}} e^{i(\boldsymbol{P}-\boldsymbol{P}')\cdot\boldsymbol{L}} J^{\tau,-\tau;v1,v2}_{\boldsymbol{P},\boldsymbol{P}';\boldsymbol{Q}}. \tag{I7}$$

Crucially, the expectation values contain information of $v1$ spins. For a magnetically disordered state, $j^{\tau,-\tau}_{\boldsymbol{R}} = 0$ and thus $\hat{x}$ and $\hat{y}$ are still degenerate. On the contrary, in the presence of a 120° coplanar spin order with sublattice magnetization m, Eq. (I5) becomes

$$\hat{H} = \hat{H}_d + mJ_{\rm exc}\sum_{\boldsymbol{R},\tau}[e^{-i\tau\boldsymbol{\kappa}\cdot\boldsymbol{R}}\hat{x}^{\dagger}_{\boldsymbol{R},\tau}\hat{y}_{\boldsymbol{R},\tau} + \text{H.c.}], \tag{I8}$$

where $\hat{H}_d$ collects all the terms diagonal in the $(\hat{x},\hat{y})$ basis. The exchange coupling constant is

$$J_{\rm exc} = \sum_{\boldsymbol{L}} e^{-i\tau\boldsymbol{\kappa}\cdot\boldsymbol{L}} J_{\boldsymbol{L},\tau}. \tag{I9}$$

Accordingly, bright and dark spectator excitons hybridize and split into two levels with a gap $\Delta_{xy} = 2m|J_{\rm exc}|$. Note that although such splitting follows from a long-range spin order,

we anticipate it to manifest even with a short-range correlation since Eq. (I8) couples only local spectator excitons.

We end this Appendix by estimating $J_{\rm exc}$. Utilizing Eqs. (I7), (H5), (H6), and (I9), this coefficient becomes

$$J_{\rm exc} = \sum_{\boldsymbol{L}} e^{-i\tau\boldsymbol{\kappa}\cdot\boldsymbol{L}} \int_{r_1,r_2} \frac{e^2 \Pi^*_{\boldsymbol{L},\tau}(\boldsymbol{r}_1)\Pi_{\boldsymbol{L},-\tau}(\boldsymbol{r}_2)}{2\epsilon_r r_{12}}, \tag{I10}$$

where the position-space pair function is

$$\Pi^*_{\boldsymbol{L},\tau}(\boldsymbol{r}) = W_{v1,\tau}(\boldsymbol{r}-\boldsymbol{L})W^*_{v2,\tau}(\boldsymbol{r}), \tag{I11}$$

with $W_{\lambda,\tau}(\boldsymbol{r})$ being the moiré-Wannier orbitals, Fourier transform of Bloch wave functions:

$$\psi_{\lambda,\boldsymbol{P},\tau}(\boldsymbol{r}) = \frac{1}{\sqrt{N}} \sum_{\boldsymbol{R}} W_\lambda(\boldsymbol{r}-\boldsymbol{R}) e^{i\boldsymbol{P}\cdot\boldsymbol{R}}. \tag{I12}$$

For further simplification, we consider tight-binding regime where moiré period is large compared to spatial extension of Wannier orbitals. In this situation, we expect the $\boldsymbol{L}=0$ term to dominate over others in Eq. (I10), giving

$$J_{\rm exc} \simeq \int_{r_1,r_2} \frac{e^2 \Pi^*_{0,\tau}(\boldsymbol{r}_1)\Pi_{0,-\tau}(\boldsymbol{r}_2)}{2\epsilon_r r_{12}}. \tag{I13}$$

Note its similarity with the direct integral for onsite Hubbard U: they both contain e^2/ϵ_r times an integral of the product of four Wannier orbitals. Thus, $J_{\rm exc}$ could in principle be comparable to U. We calculate this integral with $v1$ and $v2$ hole wave functions from the low-energy Hamiltonian below [24]:

$$\hat{H} \simeq -\frac{\hat{\boldsymbol{p}}^2}{2m^*} + \Delta(\boldsymbol{r}), \tag{I14}$$

which follows from Eq. (E1) and discussion in Appendix E. $m^* = E_l^g/2(v_l^F)^2$ is the charge effective mass. We assume $v1$ and $v2$ charges are at the same layer and hence suppress the layer index. $\Delta(\boldsymbol{r})$ is the associated moiré potential, captured by the harmonic approximation within the tight-binding regime:

$$\Delta(\boldsymbol{r})|_{\boldsymbol{r}\simeq\boldsymbol{R}} \simeq -\frac{\Delta_0}{2a_M^2}(\boldsymbol{r}-\boldsymbol{R})^2. \tag{I15}$$

We adopt $m^* = 0.35m_e$ (m_e being electron mass) and $\Delta_0 = 0.94$ eV [24] for calculation, taking $v1$ and $v2$ to be the lowest and first-excited states, respectively.

[1] J. Kang, S. Tongay, J. Zhou, J. Li, and J. Wu, Band offsets and heterostructures of two-dimensional semiconductors, Appl. Phys. Lett. **102**, 012111 (2013).

[2] D. Xiao, G.-B. Liu, W. Feng, X. Xu, and W. Yao, Coupled Spin and Valley Physics in Monolayers of MoS_2 and Other Group-VI Dichalcogenides, Phys. Rev. Lett. **108**, 196802 (2012).

[3] A. V. Stier, N. P. Wilson, K. A. Velizhanin, J. Kono, X. Xu, and S. A. Crooker, Magnetooptics of Exciton Rydberg States in a Monolayer Semiconductor, Phys. Rev. Lett. **120**, 057405 (2018).

[4] A. Chernikov, T. C. Berkelbach, H. M. Hill, A. Rigosi, Y. Li, B. Aslan, D. R. Reichman, M. S. Hybertsen, and T. F. Heinz, Exciton Binding Energy and Nonhydrogenic Rydberg Series in Monolayer WS_2, Phys. Rev. Lett. **113**, 076802 (2014).

[5] F. Wu, F. Qu, and A. H. MacDonald, Exciton band structure of monolayer MoS_2, Phys. Rev. B **91**, 075310 (2015).

[6] M. Onga, Y. Zhang, T. Ideue, and Y. Iwasa, Exciton Hall effect in monolayer MoS_2, Nat. Mater. **16**, 1193 (2017).

[7] M. Goryca, J. Li, A. V. Stier, T. Taniguchi, K. Watanabe, E. Courtade, S. Shree, C. Robert, B. Urbaszek, X. Marie, and S. A. Crooker, Revealing exciton masses and dielectric properties of monolayer semiconductors with high magnetic fields, Nat. Commun. **10**, 4172 (2019).

[8] M. Selig, G. Berghäuser, A. Raja, P. Nagler, C. Schüller, T. F. Heinz, T. Korn, A. Chernikov, E. Malic, and A. Knorr, Excitonic linewidth and coherence lifetime in monolayer transition metal dichalcogenides, Nat. Commun. **7**, 13279 (2016).

[9] G. Moody, C. Kavir Dass, K. Hao, C.-H. Chen, L.-J. Li, A. Singh, K. Tran, G. Clark, X. Xu, G. Berghäuser, E. Malic, A. Knorr, and X. Li, Intrinsic homogeneous linewidth and broadening mechanisms of excitons in monolayer transition metal dichalcogenides, Nat. Commun. **6**, 8315 (2015).

[10] K. Hao, G. Moody, F. Wu, C. K. Dass, L. Xu, C.-H. Chen, L. Sun, M.-Y. Li, L.-J. Li, A. H. MacDonald, and X. Li, Direct measurement of exciton valley coherence in monolayer WSe_2, Nat. Phys. **12**, 677 (2016).

[11] J. Li, M. Goryca, N. P. Wilson, A. V. Stier, X. Xu, and S. A. Crooker, Spontaneous Valley Polarization of Interacting Carriers in a Monolayer Semiconductor, Phys. Rev. Lett. **125**, 147602 (2020).

[12] D. K. Efimkin and A. H. MacDonald, Many-body theory of trion absorption features in two-dimensional semiconductors, Phys. Rev. B **95**, 035417 (2017).

[13] D. K. Efimkin and A. H. MacDonald, Exciton-polarons in doped semiconductors in a strong magnetic field, Phys. Rev. B **97**, 235432 (2018).

[14] T. Smoleński, O. Cotlet, A. Popert, P. Back, Y. Shimazaki, P. Knüppel, N. Dietler, T. Taniguchi, K. Watanabe, M. Kroner, and A. Imamoglu, Interaction-Induced Shubnikov–de Haas Oscillations in Optical Conductivity of Monolayer $MoSe_2$, Phys. Rev. Lett. **123**, 097403 (2019).

[15] P. Back, S. Zeytinoglu, A. Ijaz, M. Kroner, and A. Imamoğlu, Realization of an Electrically Tunable Narrow-Bandwidth Atomically Thin Mirror Using Monolayer $MoSe_2$, Phys. Rev. Lett. **120**, 037401 (2018).

[16] C. Zhang, C.-P. Chuu, X. Ren, M.-Y. Li, L.-J. Li, C. Jin, M.-Y. Chou, and C.-K. Shih, Interlayer couplings, Moiré patterns, and 2D electronic superlattices in MoS_2/WSe_2 hetero-bilayers, Sci. Adv. **3**, e1601459 (2017).

[17] F. Wu, T. Lovorn, and A. H. MacDonald, Theory of optical absorption by interlayer excitons in transition metal dichalcogenide heterobilayers, Phys. Rev. B **97**, 035306 (2018).

[18] F. Wu, T. Lovorn, and A. H. MacDonald, Topological Exciton Bands in Moiré Heterojunctions, Phys. Rev. Lett. **118**, 147401 (2017).

[19] M. H. Naik, E. C. Regan, Z. Zhang, Y.-H. Chan, Z. Li, D. Wang, Y. Yoon, C. S. Ong, W. Zhao, S. Zhao, M. I. B. Utama, B. Gao, X. Wei, M. Sayyad, K. Yumigeta, K. Watanabe, T. Taniguchi, S. Tongay, F. H. da Jornada, F. Wang, and S. G. Louie, Intralayer charge-transfer moiré excitons in van der Waals superlattices, Nature (London) **609**, 52 (2022).

[20] P. Rivera, H. Yu, K. L. Seyler, N. P. Wilson, W. Yao, and X. Xu, Interlayer valley excitons in heterobilayers of transition metal dichalcogenides, Nat. Nanotechnol. **13**, 1004 (2018).

[21] K. L. Seyler, P. Rivera, H. Yu, N. P. Wilson, E. L. Ray, D. G. Mandrus, J. Yan, W. Yao, and X. Xu, Signatures of moiré-trapped valley excitons in $MoSe_2/WSe_2$ heterobilayers, Nature (London) **567**, 66 (2019).

[22] K. Tran, G. Moody, F. Wu, X. Lu, J. Choi, K. Kim, A. Rai, D. A. Sanchez, J. Quan, A. Singh, J. Embley, A. Zepeda, M. Campbell, T. Autry, T. Taniguchi, K. Watanabe, N. Lu, S. K. Banerjee, K. L. Silverman, S. Kim *et al.*, Evidence for moiré excitons in van der Waals heterostructures, Nature (London) **567**, 71 (2019).

[23] E. M. Alexeev, D. A. Ruiz-Tijerina, M. Danovich, M. J. Hamer, D. J. Terry, P. K. Nayak, S. Ahn, S. Pak, J. Lee, J. I. Sohn, M. R. Molas, M. Koperski, K. Watanabe, T. Taniguchi, K. S. Novoselov, R. V. Gorbachev, H. S. Shin, V. I. Fal'ko, and A. I. Tartakovskii, Resonantly hybridized excitons in moiré superlattices in van der Waals heterostructures, Nature (London) **567**, 81 (2019).

[24] F. Wu, T. Lovorn, E. Tutuc, and A. H. MacDonald, Hubbard Model Physics in Transition Metal Dichalcogenide Moiré Bands, Phys. Rev. Lett. **121**, 026402 (2018).

[25] F. Wu, T. Lovorn, E. Tutuc, I. Martin, and A. H. MacDonald, Topological Insulators in Twisted Transition Metal Dichalcogenide Homobilayers, Phys. Rev. Lett. **122**, 086402 (2019).

[26] H. Pan, F. Wu, and S. Das Sarma, Band topology, Hubbard model, Heisenberg model, and Dzyaloshinskii-Moriya interaction in twisted bilayer WSe_2, Phys. Rev. Res. **2**, 033087 (2020).

[27] H. Pan, F. Wu, and S. Das Sarma, Quantum phase diagram of a Moiré-Hubbard model, Phys. Rev. B **102**, 201104(R) (2020).

[28] J. Zang, J. Wang, J. Cano, and A. J. Millis, Hartree-fock study of the moiré Hubbard model for twisted bilayer transition metal dichalcogenides, Phys. Rev. B **104**, 075150 (2021).

[29] N. C. Hu and A. H. MacDonald, Competing magnetic states in transition metal dichalcogenide moiré materials, Phys. Rev. B **104**, 214403 (2021).

[30] Y. Zhang, T. Liu, and L. Fu, Electronic structures, charge transfer, and charge order in twisted transition metal dichalcogenide bilayers, Phys. Rev. B **103**, 155142 (2021).

[31] Y. Tang, L. Li, T. Li, Y. Xu, S. Liu, K. Barmak, K. Watanabe, T. Taniguchi, A. H. MacDonald, J. Shan, and K. F. Mak, Simulation of Hubbard model physics in WSe_2/WS_2 moiré superlattices, Nature (London) **579**, 353 (2020).

[32] E. C. Regan, D. Wang, C. Jin, M. I. Bakti Utama, B. Gao, X. Wei, S. Zhao, W. Zhao, Z. Zhang, K. Yumigeta, M. Blei, J. D. Carlström, K. Watanabe, T. Taniguchi, S. Tongay, M. Crommie, A. Zettl, and F. Wang, Mott and generalized Wigner crystal states in WSe_2/WS_2 moiré superlattices, Nature (London) **579**, 359 (2020).

[33] Y. Xu, S. Liu, D. A. Rhodes, K. Watanabe, T. Taniguchi, J. Hone, V. Elser, K. F. Mak, and J. Shan, Correlated insulating states at fractional fillings of moiré superlattices, Nature (London) **587**, 214 (2020).

[34] T. Li, S. Jiang, L. Li, Y. Zhang, K. Kang, J. Zhu, K. Watanabe, T. Taniguchi, D. Chowdhury, L. Fu, J. Shan, and K. F. Mak, Continuous Mott transition in semiconductor moiré superlattices, Nature (London) **597**, 350 (2021).

[35] H. Li, S. Li, M. H. Naik, J. Xie, X. Li, E. Regan, D. Wang, W. Zhao, K. Yumigeta, M. Blei, T. Taniguchi, K. Watanabe, S. Tongay, A. Zettl, S. G. Louie, M. F. Crommie, and F. Wang, Imaging local discharge cascades for correlated electrons in WS_2/WSe_2 moiré superlattices, Nat. Phys. **17**, 1114 (2021).

[36] A. J. Campbell, M. Brotons-Gisbert, H. Baek, V. Vitale, T. Taniguchi, K. Watanabe, J. Lischner, and B. D. Gerardot, Exciton-polarons in the presence of strongly correlated electronic states in a $MoSe_2/WSe_2$ moiré superlattice, npj 2D Mater. Appl. **6**, 79 (2022).

[37] C. Jin, Z. Tao, T. Li, Y. Xu, Y. Tang, J. Zhu, S. Liu, K. Watanabe, T. Taniguchi, J. C. Hone, L. Fu, J. Shan, and K. F. Mak, Stripe phases in WSe_2/WS_2 moiré superlattices, Nat. Mater. **20**, 940 (2021).

[38] Y. Xu, K. Kang, K. Watanabe, T. Taniguchi, K. F. Mak, and J. Shan, A tunable bilayer Hubbard model in twisted WSe_2, Nat. Nanotechnol. **17**, 934 (2022).

[39] J. Choi, W.-T. Hsu, L.-S. Lu, L. Sun, H.-Y. Cheng, M.-H. Lee, J. Quan, K. Tran, C.-Y. Wang, M. Staab, K. Jones, T. Taniguchi, K. Watanabe, M.-W. Chu, S. Gwo, S. Kim, C.-K. Shih, X. Li, and W.-H. Chang, Moiré potential impedes interlayer exciton diffusion in van der Waals heterostructures, Sci. Adv. **6**, eaba8866 (2020).

[40] Z. Li, X. Lu, D. F. C. Leon, Z. Lyu, H. Xie, J. Hou, Y. Lu, X. Guo, A. Kaczmarek, T. Taniguchi, K. Watanabe, L. Zhao, L. Yang, and P. B. Deotare, Interlayer exciton transport in $MoSe_2/WSe_2$ heterostructures, ACS Nano **15**, 1539 (2021).

[41] L. Yuan, B. Zheng, J. Kunstmann, T. Brumme, A. B. Kuc, C. Ma, S. Deng, D. Blach, A. Pan, and L. Huang, Twist-angle-dependent interlayer exciton diffusion in WS_2–WSe_2 heterobilayers, Nat. Mater. **19**, 617 (2020).

[42] M. Sidler, P. Back, O. Cotlet, A. Srivastava, T. Fink, M. Kroner, E. Demler, and A. Imamoglu, Fermi polaron-polaritons in charge-tunable atomically thin semiconductors, Nat. Phys. **13**, 255 (2017).

[43] D. M. Kennes, M. Claassen, L. Xian, A. Georges, A. J. Millis, J. Hone, C. R. Dean, D. N. Basov, A. N. Pasupathy, and A. Rubio, Moiré heterostructures as a condensed-matter quantum simulator, Nat. Phys. **17**, 155 (2021).

[44] T.-S. Huang, C. L. Baldwin, M. Hafezi, and V. Galitski, Spin-mediated Mott excitons, Phys. Rev. B **107**, 075111 (2023).

[45] W. Kadow, L. Vanderstraeten, and M. Knap, Hole spectral function of a chiral spin liquid in the triangular lattice Hubbard model, Phys. Rev. B **106**, 094417 (2022).

[46] A. G. Salvador, C. Kuhlenkamp, L. Ciorciaro, M. Knap, and A. İmamoğlu, Optical Signatures of Periodic Magnetization: The Moiré Zeeman Effect, Phys. Rev. Lett. **128**, 237401 (2022).

[47] M. Azzouz and T. Dombre, Motion of holes on the triangular lattice studied using the t-*J* model, Phys. Rev. B **53**, 402 (1996).

[48] S. A. Chen, Q. Chen, and Z. Zhu, Proposal for asymmetric photoemission and tunneling spectroscopies in Fermi-Hubbard

model on triangular optical lattices, Phys. Rev. B **106**, 085138 (2022).
[49] G. Martinez and P. Horsch, Spin polarons in the t-*J* model, Phys. Rev. B **44**, 317 (1991).
[50] M. Vojta, Spin polarons in triangular antiferromagnets, Phys. Rev. B **59**, 6027 (1999).
[51] F. Grusdt, M. Kánasz-Nagy, A. Bohrdt, C. S. Chiu, G. Ji, M. Greiner, D. Greif, and E. Demler, Parton Theory of Magnetic Polarons: Mesonic Resonances and Signatures in Dynamics, Phys. Rev. X **8**, 011046 (2018).
[52] F. H. L. Essler, F. Gebhard, and E. Jeckelmann, Excitons in one-dimensional Mott insulators, Phys. Rev. B **64**, 125119 (2001).
[53] P. Wróbel and R. Eder, Excitons in Mott insulators, Phys. Rev. B **66**, 035111 (2002).
[54] E. Jeckelmann, Optical excitations in a one-dimensional Mott insulator, Phys. Rev. B **67**, 075106 (2003).
[55] Z. Alpichshev, F. Mahmood, G. Cao, and N. Gedik, Confinement-Deconfinement Transition as an Indication of Spin-Liquid-type Behavior in Na_2IrO_3, Phys. Rev. Lett. **114**, 017203 (2015).
[56] Z. Alpichshev, E. J. Sie, F. Mahmood, G. Cao, and N. Gedik, Origin of the exciton mass in the frustrated mott insulator Na_2IrO_3, Phys. Rev. B **96**, 235141 (2017).
[57] T. Terashige, T. Ono, T. Miyamoto, T. Morimoto, H. Yamakawa, N. Kida, T. Ito, T. Sasagawa, T. Tohyama, and H. Okamoto, Doublon-holon pairing mechanism via exchange interaction in two-dimensional cuprate Mott insulators, Sci. Adv. **5**, eaav2187 (2019).
[58] Equivalently, τ also labels the valley index. This is because spin and valley degrees of freedom are locked together at low energy in TMDs [20].
[59] E. C. Regan, D. Wang, E. Y. Paik, Y. Zeng, L. Zhang, J. Zhu, A. H. MacDonald, H. Deng, and F. Wang, Emerging exciton physics in transition metal dichalcogenide heterobilayers, Nat. Rev. Mater. **7**, 778 (2022).
[60] N. R. Wilson, P. V. Nguyen, K. Seyler, P. Rivera, A. J. Marsden, Z. P. L. Laker, G. C. Constantinescu, V. Kandyba, A. Barinov, N. D. M. Hine, X. Xu, and D. H. Cobden, Determination of band offsets, hybridization, and exciton binding in 2D semiconductor heterostructures, Sci. Adv. **3**, e1601832 (2017).
[61] References [31–33,36] report that exciton energy varies with filling fractions of moiré bands. They attribute this to the change in compressibility of the minibands, which implies the presence of moiré band structure despite the significant binding interaction [60]. Note that this is even more justified for excitons with higher principal quantum numbers (and hence smaller binding energies).
[62] M. Combescot, F. Dubin, and S.-Y. Shiau, Signature of electromagnetic quantum fluctuations in exciton physics, Europhys. Lett. **138**, 36002 (2022).
[63] H. Haug and S. Schmitt-Rink, Electron theory of the optical properties of laser-excited semiconductors, Prog. Quantum Electron. **9**, 3 (1984).
[64] H. Yu, G.-B. Liu, P. Gong, X. Xu, and W. Yao, Dirac cones and Dirac saddle points of bright excitons in monolayer transition metal dichalcogenides, Nat. Commun. **5**, 3876 (2014).
[65] A. Auerbach, *Interacting Electrons and Quantum Magnetism* (Springer, Berlin, 1994).
[66] X.-J. Han, Y. Liu, Z.-Y. Liu, X. Li, J. Chen, H.-J. Liao, Z.-Y. Xie, B. Normand, and T. Xiang, Charge dynamics of the antiferromagnetically ordered mott insulator, New J. Phys. **18**, 103004 (2016).
[67] M. Combescot and W. Pogosov, Composite boson many-body theory for frenkel excitons, Eur. Phys. J. B **68**, 161 (2009).
[68] Y.-H. Zhang, Doping a Mott insulator with excitons in a moiré bilayer: Fractional superfluid, neutral Fermi surface, and Mott transition, Phys. Rev. B **106**, 195120 (2022).
[69] F. Grusdt, A. Bohrdt, and E. Demler, Microscopic spinon-chargon theory of magnetic polarons in the $t-J$ model, Phys. Rev. B **99**, 224422 (2019).
[70] G. Ji, M. Xu, L. H. Kendrick, C. S. Chiu, J. C. Brüggenjürgen, D. Greif, A. Bohrdt, F. Grusdt, E. Demler, M. Lebrat *et al.*, Coupling a Mobile Hole to an Antiferromagnetic Spin Background: Transient Dynamics of a Magnetic Polaron, Phys. Rev. X **11**, 021022 (2021).
[71] Note that the facts that Mott-moiré excitons have smaller binding energy and lower dispersion than moiré excitons are not contradictory. This is because binding strength is defined as the difference between free two-particle kinetic energy and exciton dispersion. Both of these are distinct for the two types of excitons. See Appendix G for more details.
[72] V. M. Agranovich and B. S. Toshich, Collective properties of Frenkel excitons, Zh. Eksp. Teor. Fiz. **53**, 149 (1967) [Sov. Phys. JETP **26**, 104 (1968)].
[73] H. Haug and S. W. Koch, *Quantum Theory of the Optical and Electronic Properties of Semiconductors* (World Scientific, Singapore, 2004).
[74] M. Fujita, T. Nakanishi, and K. Machida, Triple-Q vortex-lattice magnetic structures of itinerant-fermion systems on a triangular lattice, Phys. Rev. B **45**, 2190 (1992).
[75] H.-Y. Yang, A. M. Läuchli, F. Mila, and K. P. Schmidt, Effective Spin Model for the Spin-Liquid Phase of the Hubbard Model on the Triangular Lattice, Phys. Rev. Lett. **105**, 267204 (2010).
[76] S. R. White and A. L. Chernyshev, Neél Order in Square and Triangular Lattice Heisenberg Models, Phys. Rev. Lett. **99**, 127004 (2007).
[77] L. Capriotti, A. E. Trumper, and S. Sorella, Long-Range Néel Order in the Triangular Heisenberg Model, Phys. Rev. Lett. **82**, 3899 (1999).
[78] T. Jolicoeur and J. C. Le Guillou, Spin-wave results for the triangular Heisenberg antiferromagnet, Phys. Rev. B **40**, 2727 (1989).
[79] J. Fröhlich and P. A. Marchetti, Slave fermions, slave bosons, and semions from bosonization of the two-dimensional t-*J* model, Phys. Rev. B **46**, 6535 (1992).
[80] S. Feng, Z. B. Su, and L. Yu, Fermion-spin transformation to implement the charge-spin separation, Phys. Rev. B **49**, 2368 (1994).
[81] A. Shimizu, K. Aoki, K. Sakakibara, I. Ichinose, and T. Matsui, Antiferromagnetic, metal-insulator, and superconducting phase transitions in underdoped cuprates: Slave-fermion t-*J* model in the hopping expansion, Phys. Rev. B **83**, 064502 (2011).
[82] D. A. Huse and V. Elser, Simple Variational Wave Functions for Two-Dimensional Heisenberg Spin-1/2 Antiferromagnets, Phys. Rev. Lett. **60**, 2531 (1988).
[83] N. Trivedi and D. M. Ceperley, Green-function Monte Carlo study of quantum antiferromagnets, Phys. Rev. B **40**, 2737 (1989).

[84] N. Bultinck, E. Khalaf, S. Liu, S. Chatterjee, A. Vishwanath, and M. P. Zaletel, Ground State and Hidden Symmetry of Magic-Angle Graphene at Even Integer Filling, Phys. Rev. X **10**, 031034 (2020).

[85] A. V. Chubukov and S. A. Kivelson, Superconductivity in engineered two-dimensional electron gases, Phys. Rev. B **96**, 174514 (2017).

[86] Y. Zeng and A. H. MacDonald, Strong modulation limit of excitons and trions in moiré materials, Phys. Rev. B **106**, 035115 (2022).

[87] D. van der Marel, Optical signatures of electron correlations in the cuprates, in *Strong Interactions in Low Dimensions*, edited by D. Baeriswyl and L. Degiorgi (Springer, Dordrecht, 2004), pp. 237–276.

[88] D. C. Mattis, The few-body problem on a lattice, Rev. Mod. Phys. **58**, 361 (1986).

[89] M. Tinkham, *Group Theory and Quantum Mechanics*, Dover Books on Chemistry and Earth Sciences (Dover, New York, 2003).

[90] We expect the exchange-induced splitting to manifest also for a variant of spectator exciton, which lies in an extra monolayer adjacent to the moiré bilayer, at temperature much lower than J. Such bound state is discussed in Ref. [33], but the temperature considered therein might not be low enough to yield the exchange-induced splitting.

[91] J. Bloch, A. Cavalleri, V. Galitski, M. Hafezi, and A. Rubio, Strongly correlated electron–photon systems, Nature (London) **606**, 41 (2022).

[92] A. Camacho-Guardian and N. R. Cooper, Moiré-Induced Optical Nonlinearities: Single- and Multiphoton Resonances, Phys. Rev. Lett. **128**, 207401 (2022).

[93] K. Slagle and L. Fu, Charge transfer excitations, pair density waves, and superconductivity in moiré materials, Phys. Rev. B **102**, 235423 (2020).

[94] Literature also report energy scales supporting Mott-insulator regime considered in this work. For example, the band gap between the first and second moiré valence bands in WSe_2/WS_2 is about 30 meV from DFT calculation [98]. This is larger than the charge gap for the correlated insulator at $\nu = -1$ in WSe_2/WS_2, experimentally estimated to be about 10∼20 meV [31].

[95] Z. Zhang, E. C. Regan, D. Wang, W. Zhao, S. Wang, M. Sayyad, K. Yumigeta, K. Watanabe, T. Taniguchi, S. Tongay, M. Crommie, A. Zettl, M. P. Zaletel, and F. Wang, Correlated interlayer exciton insulator in heterostructures of monolayer WSe_2 and Moiré WS_2/WSe_2, Nat. Phys. **18**, 1214 (2022).

[96] D. Chen, Z. Lian, X. Huang, Y. Su, M. Rashetnia, L. Ma, L. Yan, M. Blei, L. Xiang, T. Taniguchi, K. Watanabe, S. Tongay, D. Smirnov, Z. Wang, C. Zhang, Y.-T. Cui, and S.-F. Shi, Excitonic insulator in a heterojunction moiré superlattice, Nat. Phys. **18**, 1171 (2022).

[97] Y. Shimazaki, I. Schwartz, K. Watanabe, T. Taniguchi, M. Kroner, and A. Imamoğlu, Strongly correlated electrons and hybrid excitons in a moiré heterostructure, Nature (London) **580**, 472 (2020).

[98] H. Li, S. Li, M. H. Naik, J. Xie, X. Li, J. Wang, E. Regan, D. Wang, W. Zhao, S. Zhao, S. Kahn, K. Yumigeta, M. Blei, T. Taniguchi, K. Watanabe, S. Tongay, A. Zettl, S. G. Louie, F. Wang, and M. F. Crommie, Imaging moiré flat bands in three-dimensional reconstructed WSe_2/WS_2 superlattices, Nat. Mater. **20**, 945 (2021).